JCI insight

# Thrombospondin-1 promotes fibro-adipogenic stromal expansion and contractile dysfunction of the diaphragm in obesity

Eric D. Buras, … , Susan V. Brooks, Tae-Hwa Chun

*JCI Insight.* 2024. https://doi.org/10.1172/jci.insight.175047.

Research In-Press Preview Metabolism Muscle biology

## Graphical abstract

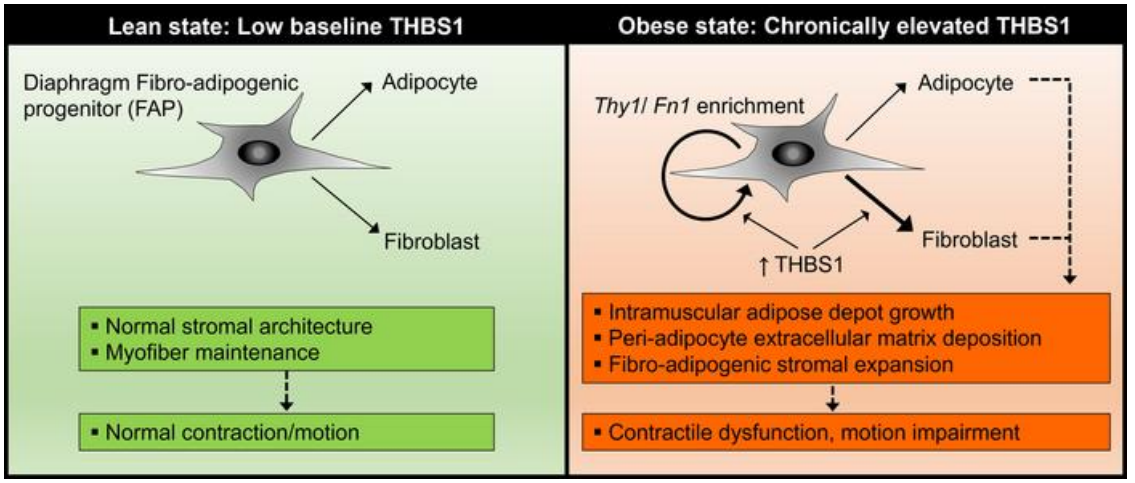

# Thrombospondin-1 promotes fibro-adipogenic stromal expansion and contractile dysfunction of the diaphragm in obesity

Eric D. Buras[1], Moon-Sook Woo[1], Romil Kaul Verma[1], Sri Harshita Kondisetti[1], Carol S. Davis[2], Dennis R. Claflin[2,3], Kimber Converso Baran[4], Daniel E. Michele[4], Susan V. Brooks[4], Tae-Hwa Chun[1,5]

[1]Division of Metabolism, Endocrinology and Diabetes (MEND), Department of Internal Medicine; [2]Department of Biomedical Engineering; [3]Department of Surgery, Section of Plastic Surgery; [4]Department of Molecular and Integrative Physiology; [5]Biointerfaces Institute, University of Michigan, Ann Arbor, Michigan, USA.

**Please address correspondence to:**

Eric D. Buras: eburas@med.umich.edu

Tae-Hwa Chun: taehwa@med.umich.edu

**Conflict of interest:** The authors have declared no conflict of interest exists.

## ABSTRACT

Pulmonary disorders impact 40-80% of individuals with obesity. Respiratory muscle dysfunction is linked to these conditions; however, its pathophysiology remains largely undefined. Mice subjected to diet-induced obesity (DIO) develop diaphragm muscle weakness. Increased intra-diaphragmatic adiposity and extracellular matrix (ECM) content correlate with reductions in contractile force. Thrombospondin-1 (THBS1) is an obesity-associated matricellular protein linked with muscular damage in genetic myopathies. THBS1 induces proliferation of fibro-adipogenic progenitors (FAPs)—mesenchymal cells that differentiate into adipocytes and fibroblasts. We hypothesized that THBS1 drives FAP-mediated diaphragm remodeling and contractile dysfunction in DIO. We tested this by comparing the effects of dietary challenge on diaphragms of wild-type (WT) and *Thbs1* knockout (*Thbs1*$^{-/-}$) mice. Bulk and single-cell transcriptomics demonstrated DIO-induced stromal expansion in WT diaphragms. Diaphragm FAPs displayed upregulation of ECM and TGFβ-related expression signatures and augmentation of a *Thy1*-expressing sub-population previously linked to type 2 diabetes. Despite similar weight gain, *Thbs1*$^{-/-}$ mice were protected from these transcriptomic changes and from obesity-induced increases in diaphragm adiposity and ECM deposition. Unlike WT controls, *Thbs1*$^{-/-}$ diaphragms maintained normal contractile force and motion after DIO challenge. THBS1 is therefore a necessary mediator of diaphragm stromal remodeling and contractile dysfunction in overnutrition and a potential therapeutic target in obesity-associated respiratory dysfunction.

## INTRODUCTION

Obesity affects over 40% of Americans (1), predisposing them to respiratory disorders that include dyspnea on exertion (DOE) and obesity hypoventilation syndrome (OHS). DOE impacts 30-80% of people with obesity, while OHS prevalence ranges from 10% in individuals with body mass index (BMI) of 30-35 kg/m$^2$ to more than 50% in those with BMI >50 kg/m$^2$ (2-11). DOE reduces the quality of life and impairs exercise tolerance (12-14), while OHS confers 5-year heart failure and mortality rates twice those of demographically matched controls (15). OHS treatment remains medically challenging. Aside from significant weight loss, chronic non-invasive positive pressure ventilation (NIPPV) is its therapeutic mainstay, and permanent tracheostomy is required in severe cases (16).

Clinical studies implicate dysfunction of the respiratory muscles—most notably the diaphragm—as a driver of obesity-associated respiratory impairment (17-20). While its underlying pathophysiology remains unclear, correlations between disordered breathing and increased limb muscle adiposity suggest diaphragm muscle quality may be compromised in people with obesity (21-23). To this end, an autopsy study identified large adipocyte inclusions in the diaphragm of an individual with OHS (24). Intriguingly, patients with obesity have significantly higher mortality rates following COVID-19 infection (25)—a condition shown to promote diaphragm fibrosis (26).

We previously applied a long-term diet-induced obesity (DIO) mouse model to define the relationship between anatomic remodeling and physiologic dysfunction of the diaphragm. In mice subjected to a 6-month high-fat diet (HFD), diaphragm contractile strength declines and inversely correlates with intramuscular adipocyte number and polymerized collagen content (27). In HFD-fed mice, platelet-derived growth factor receptor alpha (PDGFR$\alpha$)-expressing fibro-adipogenic progenitors (FAPs) are key contributors to intra-diaphragmatic accumulation of adipocytes and extracellular matrix (ECM) (27).

FAPs are mesenchymal stem cells that reside within skeletal muscle and give rise to intramuscular adipocytes and ECM-depositing cells (28-30). Important regulators of muscle

development and maintenance, FAPs orchestrate muscle stem cell (MuSC) activation and differentiation essential for tissue growth and repair (31-34). Conversely, in mouse models of muscular dystrophy (35, 36) and severe injury (32, 37), disordered FAP dynamics contribute to pathological adiposity and fibrosis associated with contractile dysfunction (38). Recent analyses using single-cell RNA-sequencing (scRNA-seq) demonstrate distinct FAP populations with pro-remodeling and pro-adipogenic potentials (39). Furthermore, a specific FAP subset marked by *THY1* (CD90) expression was associated with fibro-fatty degeneration in quadriceps muscles of individuals with type 2 diabetes (40). Despite these recent advances, molecular mechanisms underlying FAP dysregulation in obesity remain largely unknown.

Thrombospondin-1 (THBS1 or TSP-1) is a matricellular protein present in tissues and circulation. In humans, serum THBS1 levels increase with body mass index (BMI) and are associated with adipose inflammation, insulin resistance, and diabetes (41-44). In mice, *Thbs1* ablation protects against HFD-induced adipose fibrosis while reducing collagen deposition in limb muscles (45). In vitro, THBS1 induces the proliferation of bone marrow-derived mesenchymal cells by activating TGFβ (46). Furthermore, local and circulating THBS1 contribute to fibrotic and degenerative changes in heritable myopathies (47, 48). We previously demonstrated that THBS1 circulates at high levels in mice subjected to DIO (27, 45) and induces the proliferation of diaphragm FAPs (27). Therein, THBS1 is a putative regulator of FAP phenotype and consequent diaphragm remodeling in obesity.

Using the *Thbs1*-null state as an interrogating probe, we aimed to identify FAP subtypes involved in obesity-induced diaphragm remodeling and determine whether *Thbs1* ablation could ameliorate attendant contractile impairment. Our findings indicate that *Thbs1* plays a crucial role in activating TGFβ signaling in diaphragm FAPs and expanding a $THY1^+$ FAP subtype. *Thbs1* knockout mice are protected from obesity-induced fibro-adipogenic diaphragm remodeling and respiratory dysfunction.

## RESULTS

***Diaphragm FAP transcriptomic profile and sub-populations change in response to diet-induced obesity:*** scRNA-seq has shown FAPs to be a heterogeneous cell type with functionally relevant sub-populations that expand and contract in response to denervation, muscular dystrophy, and injury (34, 49, 50). Transcriptomic changes underlying obesity-associated diaphragm remodeling, on the other hand, remain undefined. To analyze these, we applied scRNA-seq to mononuclear isolates from costal diaphragms (excluding central tendon and rib attachments) of male C57BL/6J mice subjected to 6-month control diet (CD) (n= 2) or HFD (n= 2) feeding. We computationally aggregated 10X Genomics data to produce a dataset comprising $3.4x10^8$ reads over 7,906 cells. These resolved into populations MuSCs (expressing *Myf5*, *Pax7,* and *Cdh15*), endothelial cells (expressing *Flt1*, *Pecam1,* and *Ptprb1*), lymphatic cells (expressing *Clca3a1*, *Ccl21a,* and *Mmrn1*), Schwann cells (expressing *Mpz*, *Ncma*p, and *Kcna1*) and macrophages (Mϕs—expressing *Itgam*, *Cd68,* and *Lyz2*); as well as a heterogeneous leukocyte cluster containing lymphocytes and eosinophils (Figure 1A, S1A). FAPs—identifiable based on their expression of *Pdgfra*, *Pdgfrb*, *Dcn*, and *Osr1* (29, 51)—were the dominant costal diaphragm cell type, accounting for >50% of sequenced events (Fig 1A-B, S1A). A small mesothelial population (with unique enrichment of *Msln*, *Lrn4,* and *Upk3b*) also expressed *Osr1* and *Dcn* but lacked *Pdgfra* and *Pdgfrb* (Figure 1B, S1A).

To interrogate their heterogeneity, we re-clustered FAPs (4,171 cells) into five sub-populations (Figure 1C-D). The largest of these, FAP1, was enriched in transcripts encoding *G0s2*, *Hsd11b1*, *Vtn,* and *Ccl11* (Figure 1D, S1B-C). This expression signature overlaps with that of the *Cxcl14*-expressing FAP subset previously identified in mouse gastrocnemius and tibialis anterior muscle (52, 53), and closely resembles that of the “adipocyte progenitors” defined by Hepler et al. on scRNA-seq analysis of PDGFR$\beta^+$ cells from mouse adipose tissue (54). Consistent, cells expressing *Mme*—a newly defined marker of adipogenic FAPs (55)—were

restricted to FAP1 (Fig S1C). Few FAPs in any sub-cluster expressed *Cebpa, Pparg,* or *Adipoq* (S1D), indicating that the diaphragm FAP pool contains numerous adipocyte progenitors but few committed preadipocytes.

Cells within FAP2 expressed the established FAP marker *Fbn1,* in addition to *Limch*, *Efhd1*, *Smn4*, *Has2*, *Cmah* and *Dact2* (Figure 1D, S2A-C). The latter signature is consistent with the non-adipogenic, ECM-depositing "fibroinflammatory progenitor" previously described in adipose tissue (54). In agreement, FAP2 cells were enriched in the transcript encoding fibronectin (*Fn1*) (Fig S2C). Moreover, FAP2 profile broadly overlapped with that of FBN1$^{+}$ and *Cd55*-expressing FAP populations, respectively identified in mouse and human skeletal muscles (51, 55) (Fig S2A). FAP2 cells demonstrated enhanced expression of the genes encoding DPP4 (*Dpp4*) (Fig S2B)—an adipose stem cell marker (56) that also identifies *Cxcl14*-negative FAPs (52, 53)—and endosialin (*Cd248*) (Fig S2D), an obesity-associated glycoprotein (57).

Cells within FAP3 highly expressed *Timp1*, a key autocrine regulator of mesenchymal stem cell identity (58). FAP3 cells were further enriched in transcripts expressed within the FAP5 sub-population, such as that encoding the sulfotransferase SULT1E1 (*Sult1e1*) (Figure 1D, S3A-B). Cells within FAP4 had a more specific signature, expressing transcripts encoding secreted regulators of MuSC differentiation, including the small interstitial leucine-rich proteoglycan fibromodulin (*Fmod*) and soluble Wnt signaling modulator SFRP2 (*Sfrp2*) (59, 60). While FAP4 uniquely contained cells that expressed tenomodulin (*Tnmd*), none within the population expressed the tenocyte marker scleraxis (*Scx*) (61, 62) (Figure 1D, S3C-D).

To assess the impact of dietary modification on the diaphragm FAP population, we analyzed differential gene expression between diaphragm FAPs from CD and HFD-fed mice. Consistent with our previous work—which showed some diaphragm FAPs to assume a pro-fibrotic phenotype in the setting of DIO (27)—FAPs from HFD samples exhibited enhanced expression of genes encoding ECM species, such as *Col3a1*, *Col5a2*, *Col5a3,* and *Col6a3* (Figure 1E). In addition, HFD FAPs were enriched in FAP2 transcripts—*Fbn1*, *Pla1a1*, *Sema3c*,

*Cd55*, *Mfap5* and *Thy1* (Figure 1E, S2A, C). The latter was particularly intriguing, given a recent report describing an increase in THY1$^+$ FAPs in obese individuals with type 2 diabetes, who demonstrate fibro-fatty muscle degeneration (40). In our dataset, *Thy1* transcript was largely restricted to FAP2 (Figure 1F-G), while *Thy1*-expressing cells likewise expressed FAP2 marker genes (Figure S4A-B). Notably, *Thy1*-expressing FAPs were more numerous in samples from mice fed HFD than CD (Fig 1H).

Taken together, these data demonstrate that diaphragm FAPs resolve into distinct sub-populations, suggesting compartmentalization of adipogenic, ECM-deposition, and regulatory functions. HFD promotes a pro-fibrotic transcriptomic signature and FAP2 subpopulation enrichment, with a corresponding increase in *Thy1*-expressing cells. These findings corroborate our earlier demonstration of increased fibrogenic FAPs within the obese diaphragm (27) while revealing similarities between the diaphragms of DIO mice and limb muscles of obese human subjects with type 2 diabetes (40).

***THBS1 underlies quantitative and qualitative changes in diaphragm FAPs during the DIO challenge:*** We next sought to identify molecular regulators of DIO-induced FAP profile changes; and focused on the obesity-associated growth factor THBS1 (27, 44-46). To ascertain its impact on FAP biology in vitro, we isolated FAPs with fluorescence-activated cell sorting (FACS) using an established surface marker profile (Sca-1$^+$, CD31$^-$, CD45$^-$, integrin $\alpha$7$^-$) (28, 29) then applied THBS1 at a concentration observed in the plasma of human subjects with obesity (44). THBS1 administration induced FAP proliferation, as indicated by increased number of Ki67-labeled cells (Figure 2A). Furthermore, THBS1-treated cells demonstrated enhanced extracellular deposition of FAP2-associated fibronectin (Figure 2B).

Given the high level of circulating THBS1 in HFD-fed mice (27), we hypothesized that THBS1 contributed to DIO-associated FAP changes in the diaphragm. To test this, we subjected whole-body *Thbs1* knockout (KO) mice (45) (Figure S5A-B) and wild-type (WT) controls to 6-

month HFD-feeding, then evaluated diaphragm FAPs by flow cytometry, immunohistochemistry (IHC) and scRNA-seq.

As previously reported (43), KO mice displayed slightly reduced linear body growth during adulthood versus WT animals (Figure S5C). Nonetheless, they gained weight with HFD feeding (Figure S5D-E) such that their body composition was equivalent to that of HFD-fed WT mice (Figure S5F). Additionally, both WT and KO mice fed HFD showed similarly impaired glucose tolerance compared to age-matched WT mice fed CD (Figure S5G). WT and KO animals also demonstrated comparable DIO-induced increases in liver, perigonadal adipose, and inguinal adipose weights (Figure S6A-C). Finally, weights of several limb muscles did not significantly differ between groups regardless of diet (Figure S6D-H).

Using flow cytometry, we compared mononuclear isolates (two whole costal diaphragms—excluding central tendon and rib attachment—per sample) from WT and KO mice fed either CD or HFD for six months (n= 3-6 samples per group); and quantified FAPs per mg tissue. In WT mice, FAP quantity increased with HFD feeding. On the contrary, KO mice had an equivalent FAP number per mg tissue, regardless of dietary condition (Figure 2C). We corroborated these findings by performing IHC for FAP marker PDGFR$\alpha$ on frozen costal diaphragm samples (n= 5-8 animals per group)—observing HFD-induced FAP number increase within WT but not KO mice (Figure 2D). We then asked whether KO mice were also protected from DIO-induced changes in FAP transcriptomics. To assess this, we integrated samples from 6-month HFD-fed KO animals into our scRNA-seq framework. In diaphragm mononuclear isolates from WT CD (n= 2), WT HFD (n= 2) and KO HFD (n= 2) mice ($5.2 \times 10^8$ reads over 12,275 cells), we focused our attention on FAPs (6,591 cells). Velocity analysis of these data demonstrated DIO to induce differentiation from *Timp1*-expressing FAP3 progenitors toward FAP2. In WT mice, this produced a quantitative increase in the FAP2 population, and a commensurate increase in *Thy1*-expressing cells (Fig 3A). In contrast, HFD-fed KO mice were protected from these population shifts and maintained FAP2 and *Thy1*-expressing cell content like that of WT mice fed CD (Figure 3A). In agreement,

194 total FAP samples from WT HFD mice showed selective enrichment of marker genes for FAP2
195 (Figure 3B) and *Thy1*-expressing cells (Figure S7A).

196 We next used iPathwayGuide to examine genes and biological pathways enriched in each
197 group (Figure S7B). Several ECM-related genes—*Adamts5*, *Sema3c*, *Itih5*, *Cd55*, *Fbn1*, *Col3a1*,
198 *Col4a1*, *Col4a2* and *Col6a3*—were upregulated in both HFD-fed WT and KO FAPs compared to
199 those of WT mice fed CD—however, their expression levels were highest in WT HFD samples
200 (Figure S7C). Genes with specific upregulation in the WT HFD group included those encoding
201 proteins involved in TGF-β signaling and myofibroblastic transition (e.g. *Zeb1*, *Tgfbr2* and *Prg4*)
202 (63-65) (Figure 3C, S7D-E). In agreement, numerous TGF-β-associated pathways were enriched
203 in WT HFD (Figure 3D, S8A) but not in WT CD or KO HFD samples (Figure S8A-E). Given these
204 findings, we sought to determine whether the mitogenic impact of THBS1 on FAPs (Figure 2A-B)
205 depended on TGFβ. Indeed, we observed that co-treatment with SB-431542, an inhibitor of TGFβ
206 signaling (66), ameliorated THBS1-induced FAP proliferation, while dramatically inhibiting
207 fibronectin deposition (Fig S9A-C).

208 We then analyzed TGFβ receptor expression within FAP subtypes and found *Tgfbr2* to be
209 enriched in FAP2. On the contrary, other transcripts encoding receptors for TGFβ and PDGF
210 species (i.e. *Tgfbr1*, *Tgfbr3*, *Pdgfra* and *Pdgfrb*) were expressed equally across FAP populations
211 (Figure S10A-B). Interestingly, the gene encoding CD47—a cell surface THBS1 receptor that acts
212 as a “don’t eat me signal” to inhibit Mϕ-mediated phagocytosis of fibroblasts and other cell types
213 (67)—was also enriched in FAP2 (Figure S10C). Conversely, the gene encoding established
214 endothelial THBS1 receptor, CD36 (68), was negligibly expressed in FAPs of all subtypes (Figure
215 S10C).

216 Together, these data demonstrate that THBS1 is required for DIO-induced expansion of
217 FAP pool and its shift toward *Thy1*-expressing, FAP2 cells. Increased TGF-β signaling—known

to be activated by THBS1 (46) and elevated in DIO (69)—likely underlies key aspects of this phenotypic switch.

***Whole tissue transcriptomics highlights reduced stromal gene expression in obese Thbs1$^{-/-}$ mice:*** To determine whether FAP profile differences between HFD-fed WT and KO mice corresponded with gene expression changes at the tissue level, we performed bulk RNA-seq on whole costal diaphragm samples (n= 3 diaphragms per group) from these animals. This analysis revealed a pronounced difference in the transcript encoding adipocyte marker leptin (*Lep*)—expressed more in WT samples (Figure 4A). We performed an integrated analysis to determine whether other differentially expressed transcripts identified by bulk RNA-seq were enriched in any of the specific mononuclear cell types defined by scRNA-seq. This approach showed that numerous genes more highly expressed in HFD-fed WT diaphragm tissue were specifically enriched in FAPs (*Mfap5*, *Dpt*, *Fbn1*, *Cilp*, *Fn1*, *Pmepa1*, *Ctgf*, *Sod3* and *Prg4*) and Mϕs (*S100a4*, *C1qb*, *Ccl6*, *Ctss*, *C1qa*, *Pf4*, *Cd44*, *F13a1*, *Cd68*, and *Plin2*) (Figure 4A-B). On the contrary, (aside from Schwann cell marker *Mpz*) transcripts enriched in HFD-fed KO samples were not enriched in any mononuclear cell type. In fact, genes relatively overexpressed in the KO diaphragm included well-known myofiber transcripts, like those encoding parvalbumin (*Pvalb*) and alpha-actinin-3 (*Actn3*) (Figure 4A-B). Consistent with this, GSEA demonstrated the HALLMARK epithelial to mesenchymal transition pathway (which contains ECM-related genes) and inflammatory response pathway (which contains Mϕ-related genes) to be enriched more in WT than KO samples (Figure 4C). Quantitative PCR (qPCR) analysis substantiated these findings, showing *Thbs1* ablation to reduce levels of *Lep*, *Pdgfra*, *Fn1* and *Col3a1* in diaphragms of HFD-fed mice (Fig 4D).

Expression of *Emr1*, encoding Mϕ marker F4/80, also trended down in KO samples; however, the difference did not reach statistical significance (Figure 4D). CD68

immunohistochemistry on costal diaphragm sections further demonstrated HFD feeding to raise tissue Mϕ number in WT mice. This increase was less pronounced in KO animals (Figure S11A); however, total Mϕ number, even in WT HFD-fed mice, was 2-3 fold lower than that of FAPs (Figure 2C). Furthermore, analysis of scRNA-seq data showed lipid-associated *Trem2*-expressing Mϕs (70) to exist in equal proportion in samples from HFD-fed WT and KO mice (Figure S11B).

Taken together, these data show *Thbs1* ablation reduces expression of stromal genes—particularly those specific to adipocytes, FAPs and Mϕs—in the obese diaphragm. Of the latter two cell types, FAPs are likely greater contributors to tissue-level phenotype, given their higher numbers. The relative increase in muscle-specific transcripts within the KO diaphragm suggests an increased muscle/ stroma ratio in the setting of *Thbs1* ablation.

***Thbs1 ablation protects against diaphragm fibro-adipogenic remodeling:*** We previously demonstrated that DIO promotes diaphragm tissue remodeling, characterized by increased FAP-derived ECM-depositing cells and intramuscular adipocytes (27). Given that *Thbs1* ablation ameliorated FAP population expansion and subtype shifts while reducing adipocyte and ECM-related transcripts, we surmised that KO mice would be protected from the remodeling phenotype.

To assess this, we examined tissue morphology in H/E-stained longitudinal costal diaphragm sections spanning the rib and tendon attachment points (n= 5-7 mice per group, 3-4 non-consecutive sections per animal) (Figure 5A). In WT mice, this analysis demonstrated intramuscular adipocyte inclusions—their identity confirmed by staining for the lipid droplet protein perilipin (Fig S12A)—that were particularly prominent in the lateral costal diaphragm and larger in mice subjected to 6-month DIO (Figure 5A). Indeed, intramuscular adipocyte size and number; as well as tissue cross-sectional area occupied by adipocytes, increased in HFD- versus CD-fed

267 animals (Fig 5B, S12A). Despite similar weight gain to WT mice, KO mice were largely protected
268 from obesity-associated intramuscular adiposity (Figure 5A-B, S12A).

269 We next sought to understand the geographical relationship between these intramuscular
270 adipose depots and THY1$^+$ FAPs. Immunofluorescent staining of adjacent sections for perilipin
271 and THY1 demonstrated collections of THY1$^+$ cells close to adipocyte inclusions—their number
272 higher in HFD-fed WT samples versus the other groups (Figure 5C). Moreover, prominent
273 deposition of both fibronectin (Figure 5D) and polymerized collagen (Figure 5E) surrounded
274 adipose depots. Both increased with HFD-feeding in WT mice, while samples from HFD-fed KO
275 mice resembled those of WT mice fed CD. Consistent with the higher expression of *Col3a1* in
276 HFD-fed WT versus KO tissue, intra-diaphragmatic collagen 3 deposition also increased with DIO
277 in a *Thbs1*-dependent manner (Fig S12B).

278 We next examined a diaphragm autopsy sample from a 62-year-old individual with obesity
279 (BMI 32 kg/m$^2$) and observed rests of intramuscular adipocytes akin to those seen in diaphragms
280 of WT HFD-fed mice (Fig S12C). These intramuscular depots were larger than those seen in a
281 sample from a 72-year-old individual of normal BMI (22 kg/m$^2$)—and, like in the DIO mouse model,
282 associated with areas of increased fibronectin deposition and THY1$^+$ cells (Fig S12D).

283 Notably, diaphragm samples from HFD-fed WT and KO mice did not significantly differ in
284 thickness (Figure S13A), myofiber cross-sectional area (Figure S13B), or myofiber type (Figure
285 S13C). Together, these histological analyses provide evidence that *Thbs1* ablation protects the
286 diaphragm from DIO-induced fibro-adipogenic remodeling in a manner consistent with the effects
287 predicted from transcriptomic profiles at the cell and tissue level. Moreover, the findings indicate
288 that DIO-induced, *Thbs1*-dependent increases of intramuscular adiposity are geographically
289 coupled with ECM deposition and abundant THY1$^+$ cells in a pattern that resembles the histology
290 of the obese human diaphragm.

291

***The Thbs1$^{-/-}$ diaphragm preserves its contractile force in the setting of DIO challenge:*** Given the improved tissue architecture observed in HFD-fed KO versus WT mice, we predicted that *Thbs1* ablation would also protect the diaphragm from obesity-associated mechanical dysfunction. To test this hypothesis, we performed *ex vivo* isometric force testing on diaphragm strips (Figure S13D) isolated from WT and KO mice at baseline (2-months old) and following 6-month CD or HFD feeding (n= 4-6 mice per group, 1-2 diaphragm samples per mouse). In WT animals, 6-month CD effected no difference in isometric force versus baseline. HFD, on the other hand, caused specific force to decline by nearly 20% (Figure 6A). In KO mice, specific force values remained unchanged from baseline regardless of whether animals received CD or HFD (Figure 6A). In addition, samples from 6-month HFD-fed KO mice had significantly higher specific force measurements than those of HFD-fed WT mice. (Figure 6B). Therefore, *Thbs1* ablation protects the diaphragm from obesity-associated contractile force reduction.

Within diaphragm muscle strips from HFD-fed WT and KO mice subjected to isometric testing, we observed a negative correlation between adipocyte-occupied cross-sectional area and measured specific force (Figure 6C). Given this relationship, we surmised that tissue-level contractile force deficits resulted from altered muscle architecture. An alternative explanation is that THBS1 could directly impair myofiber function in obesity. To test this possibility, we performed isometric force testing on single myofibers isolated from WT and KO mice fed HFD for 6 months (Figure 6D). This analysis found specific force measurements of individual fibers from mice of each group to be statistically indistinguishable (Figure 6E, S13E). As such, the protective effect of *Thbs1* ablation is not dependent on better sarcomere contractility, but instead may result from undisrupted tissue architecture necessary for coordinated muscle contraction.

***Thbs1 ablation protects mice from obesity-associated deterioration of diaphragm motion:*** We then asked whether the preservation of normal diaphragm contraction seen in HFD-fed KO mice translated into protection from obesity-associated respiratory dysfunction. To assess

this, we subjected WT and KO to a 6-month HFD time course and serially analyzed diaphragm motion with non-invasive ultrasound. M-mode measurements—plotted with time on the x-axis and diaphragm displacement on the y-axis—enable measurement of diaphragm excursion amplitude, inspiratory velocity, and expiratory velocity (Figure 6F) (27, 71). In WT mice, these parameters progressively declined with HFD feeding duration. On the contrary, in KO mice, all measurements remained stable throughout the time course (Figure 6G-I). Moreover, at the 6-month time point, baseline-normalized amplitude, inspiratory velocity, and expiratory velocity were significantly higher in KO than WT mice (Figure 6G-I). In sum, animals lacking *Thbs1* are protected from obesity-associated diaphragm motion compromise.

## DISCUSSION

Our findings demonstrate that anatomic remodeling and contractile dysfunction of the diaphragm are interrelated, *Thbs1*-dependent obesity complications. In the setting of long-term overnutrition, THBS1 promotes stromal expansion characterized by increased $THY1^+$ FAPs, aberrant ECM deposition and elevated intramuscular adiposity. These changes correspond with a decline in tissue-level isometric force generation—independent of single myofiber sarcomere function—contributing to reduced diaphragm motion.

Our results define THBS1 as a key regulator of quantitative expansion and qualitative changes in the diaphragm FAP pool during long-term DIO. A circulating matricellular protein, THBS1 is produced by megakaryocytes, platelets, leukocytes, endothelial cells, fibroblasts, and adipocytes (41, 72-74). In most cell types, THBS1 expression is low at baseline but acutely rises in wound healing and ischemic stress responses (75). Persistent, maladaptive THBS1 elevation occurs with aging and prolonged nutritional stress. For instance, *THBS1* expression increases in adipose depots of obese human subjects and positively correlates with the degree of insulin resistance (41); while plasma THBS1 concentrations are higher in patients with impaired glucose

343 tolerance (44, 76). Rodent metabolic syndrome models recapitulate these findings (45), as
344 evidenced by increased circulating THBS1 levels observed in DIO mice (27, 45).

345 Deposited in the ECM, THBS1 induces context-specific trophic effects—both proliferation
346 and ECM production—on stromal cells (75). In cultured bone marrow-derived mesenchymal cells,
347 THBS1 acts as a potent mitogen (46). Our in vitro data demonstrate an analogous effect on FAPs,
348 as THBS1 concentrations comparable to those found in human subjects with obesity (44) promote
349 their proliferation. Analysis of FAPs from diaphragms of KO mice supports the relevance of this
350 effect in vivo: Unlike WT mice, which undergo expansion of the FAP pool with obesity, KO mice
351 maintain similar FAP numbers to baseline when challenged with DIO. Mechanistically, THBS1
352 induces established FAP mitogens—specifically facilitating the conversion of latent to active
353 TGFβ (46). Our transcriptomic analyses and in vitro experiments highlight TGFβ as a likely driver
354 of *Thbs1*-dependent FAP proliferation. These data further implicate THBS1 in the augmented
355 TGFβ signaling previously described in human subjects with metabolic syndrome (77). Of note,
356 parallel impacts of THBS1 on other trophic factors or FAP survival (32, 40, 78)—for instance, via
357 reduced Mϕ-mediated clearance (67)—might also regulate diaphragm FAP pool size.

358 THBS1 promotes mesenchymal ECM production in numerous tissues (79)—and this
359 process appears operative in diaphragm FAPs. In vitro, THBS1 induces deposition of fibronectin,
360 an ECM molecule transcriptionally regulated by TGFβ (80). In vivo, FAPs isolated from the obese
361 diaphragm assume a fibrogenic signature. THBS1 is required for this shift, since the expression
362 of numerous obesity-induced, ECM-realted FAP genes (such as *Fbn1*, *Col3a1* and *Adamts5*) is
363 markedly blunted in HFD-fed KO mice. Moreover, some of the genes most upregulated in WT
364 HFD versus WT CD and KO HFD FAPs include species involved in TGFβ signaling (e.g. *Zeb1*,
365 *Tgfbr2* and *Prg4*).

366 scRNA-seq-based sub-clustering defined several diaphragm FAP subpopulations; some
367 exhibiting considerable transcriptomic overlap with those described previously. The most notable

368 was *Thy1*-expressing FAP2—a cell type similar to the fibroinflammatory progenitor described in
369 visceral and subcutaneous adipose tissue and the FBN$^+$ and *Cd55*-expressing FAP subsets
370 identified in human and mouse skeletal muscle (51, 54, 55). In our model, the FAP2 population
371 arose from *Timp1*-expressing FAP3 precursors and expanded with DIO, shifting the total FAP
372 pool toward enrichment of FAP2 markers. We noted a striking resemblance between FAP2 and
373 the THY1$^+$ FAPs previously shown to increase in individuals with type 2 diabetes. In these human
374 samples, the presence of THY1$^+$ cells was associated with fibro-fatty muscle remodeling (40) like
375 that seen in DIO mice (27) and our diaphragm autopsy samples. Furthermore, THY1$^+$ FAPs have
376 been associated with tissue-level fibrosis in the context of denervation (34); though not in
377 Duchenne muscular dystrophy, in which an *Adam12*/ *Mmp19*/ *Postn*-expressing sub-population
378 (without a clear analog in our dataset) appears to be a dominant contributor (53).

379 THBS1 promotes FAP proliferation and expansion of the overall FAP pool while
380 particularly impacting the FAP2 sub-population. Indeed, subtype profile and velocity plots of FAPs
381 from HFD-fed KO mice did not demonstrate FAP2 enrichment and, indeed, were nearly
382 indistinguishable from those of CD-fed WT mice. Dietary condition and *Thbs1* ablation had little
383 impact on the relative size of the FAP1 subpopulation—an analog of previously described
384 adipocyte progenitors (54). The observed FAP profiles, therefore, align with our previous findings:
385 While DIO induces both increased intra-diaphragmatic adiposity and fibrosis, FAPs isolated from
386 the obese diaphragm do not display enhanced ex vivo adipogenesis but do exhibit upregulated
387 ECM deposition. As such, increased intramuscular adipocyte number likely results from increased
388 FAP number (27) and/ or THBS1-dependent tissue remodeling, creating a microenvironment
389 permissive for adipocyte differentiation and expansion in vivo.

390 On the whole, THBS1 facilitates obesity-associated expansion of the diaphragm FAP pool,
391 inducing a fibrogenic transcriptomic signature typified by TGFβ-dependent gene expression and
392 enrichment of a THY1$^+$ subpopulation previously linked to tissue-level remodeling. Given its
393 multiple potential cells of origin, delineating the specific source of THBS1 responsible for the

phenotype—and whether it reaches the diaphragm through circulation or from nearby adipose depots—is an important area of future investigation.

During a 6-month DIO time course, the diaphragm undergoes progressive anatomic remodeling characterized by increased intramuscular adiposity and ECM deposition (27). Here, we show that adipocytes in DIO mice are not uniformly distributed throughout the costal diaphragm tissue but instead exist largely in aggregations close to the rib attachment point. ECM distribution is also not homogenous, as densities of polymerized collagens and fibronectin often appear closely interposed with adipocytes. Similarly, THY1$^+$ cells preferentially congregate near these intramuscular adipose depots, demonstrating a coupling of their presence and fibro-fatty expansion. *Thbs1* is an essential mediator of these processes, given that KO mice are protected from adipose depot expansion and the associated increase in THY1$^+$ FAPs and ECM deposition.

Tissue-level transcriptomic analysis substantiates these histological findings, showing that, compared to the HFD-fed WT diaphragm, the HFD-fed KO diaphragm displays reduced expression of numerous stromal genes—particularly those associated with adipocytes and ECM-depositing FAPs (e.g. *Lep*, *Fn1*, *Fbn1*, *Prg4* and *Mfap5*). Conversely, transcripts more highly expressed in the HFD-fed KO diaphragm include those specific to the myofiber (e.g. *Actn3* and *Pvalb*). This raises questions as to whether increases in myofiber-specific transcripts in the obese KO diaphragm are relative—i.e. occurring because there is less stromal tissue than in the obese WT diaphragm—or represents a protective effect of *Thbs1* ablation on myofiber preservation during overnutrition. Our histological data supports the former possibility, as diaphragm thickness, myofiber size and myofiber type are unchanged between diaphragms of HFD-fed WT and HFD-fed KO mice. Moreover, compared to diaphragms of CD-fed WT mice, the WT HFD diaphragm does not display pathological hallmarks of atrophy (centrally nucleated or angular myofibers) (27).

THY1$^+$ FAPs are predominantly fibrogenic and contribute to the deposition of fibronectin and other ECM species near adipose depots (40, 54). Delineating other roles they might play in tissue-level remodeling—e.g. differentiation into adipocytes (55) or secondary promotion of

adipose depot expansion through inhibition of myofiber maintenance—are important future directions.

Our current findings apply only to male mice. Subsequent studies, including both male and female animals, will be required to determine whether any aspects of obesity-associated diaphragm remodeling or FAP complement are sexually dimorphic (81)—a critical issue given recent reports of estradiol signaling to promote pro-fibrotic responses in *Pdgfra*-expressing mesenchymal cells of the abdominal wall musculature (82). Additionally, future application of a micronutrient-matched control diet in parallel to standard chow can definitively rule out any impact of small vitamin and mineral concentration differences on the observed phenotypes.

Finally, while the single obese human diaphragm sample evaluated in this study contains large intramuscular adipose depots surrounded by fibronectin and THY1-immunopositive stromal cells, further analysis of human samples from individuals with normal and elevated BMI is required to determine the degree to which our animal model findings can be translated to humans—a key point given potential inter-species differences in intramuscular adiposity (83).

Our testing of isometric specific force in isolated diaphragm strips demonstrates that 6-month DIO markedly impairs contractile function. The process depends on *Thbs1*, as diaphragm samples from KO mice subjected to the same diet maintain equivalent specific force versus baseline and demonstrate significantly greater force than isolates from HFD-fed WT mice. In contrast, measurements of specific force in single myofibers isolated from HFD WT and HFD KO mice exhibit no difference between groups. This data can be interpreted as demonstrating that obesity-induced isometric force deficits result from tissue-level remodeling rather than myofiber dysfunction. We note that single fiber force testing must be performed on permeabilized myofiber segments. While fresh, intact myofibers can be isolated from small murine muscles like the lumbrical (84), the procedure is not technically feasible in larger muscles like the diaphragm (D. Claflin, unpublished observations). Consequently, the single myofiber approach tests the

functional integrity of the sarcomere but may exclude the assessment of extrinsic regulation of excitation-contraction coupling (85).

Despite these caveats, augmentation of intramuscular adipose depots likely plays a substantial role in diminution of diaphragm isometric force during overnutrition. For instance, in well-defined models of simultaneous intramuscular adiposity and contractile dysfunction (such as chemical injury of the EDL) lipodystrophic mice unable to generate adipocytes are protected from post-injury isometric force deficits (38). As we previously described in the obese diaphragm and again demonstrate here, the authors of the aforementioned study found that simple occupation of muscle cross-sectional area by adipocytes was insufficient to quantitatively account for the measured isometric specific force reduction in wild type mice (38). Together, these findings suggest that a negative impact of intramuscular adipose depots on contractile physiology may be exerted through disruption of normal tissue architecture or via paracrine signaling to myofibers (86). Clinical relevance is highlighted by reports linking reduced limb muscle density (computed tomography), indicative of elevated intramuscular adiposity, to reduced physical performance in elderly men (87) and impaired lung function in young adults with obesity (23).

In our study, *Thbs1*-dependent fibro-adipogenic remodeling and contractile dysfunction correspond with compromised diaphragm motion on non-invasive ultrasound—highlighting the manifestation of THBS1-driven changes in clinically measurable outcomes. Blockade of THBS1 has been shown to mitigate hyperglycemia-induced peritoneal fibrosis (88), while inhibition of THBS1-dependent TGFβ activation reduces renal injury and proteinuria in mouse models of diabetic nephropathy (89). To this end, pharmacological targeting of THBS1 and its downstream signaling pathways may hold potential as a treatment for obesity-associated respiratory dysfunction.

## METHODS

***Sex as a biological variable:*** Male mice were used for the study to obviate any confounding effect of variable estrogen levels on FAP biology (82). Diaphragm tissue from human female subjects of postmenopausal age revealed similar obesity-induced remodeling to that seen in male DIO mice.

***Animals:*** Wild type C57BL/6J (#000664) and *Thbs1*$^{-/-}$ mice (#006141) were obtained from The Jackson Laboratory (Bar Harbor, ME). Jackson maintains *Thbs1*$^{-/-}$ mice on a C57BL/6J background. Animals were housed in pathogen-free containment with a 12-hour light-dark cycle and *ad libitum* food and water. For DIO studies, mice received a normal chow diet (5L0D; LabDiet, St Louis, MO) until 2 months of age. CD-fed mice continued this for an additional 6 months, while HFD-fed mice switched to a diet containing 45% calories from lipid (D12451; Research Diets, New Brunswick, NJ) and subsequently maintained this for 6 months. Body composition was assessed via NMR (using the EchoMRI 4in1-500). Glucose tolerance testing was performed via intraperitoneal injection of a 10% dextrose solution (in sterile water) dosed at 1g/ kg total body weight. Glucose measurements were made using a One Touch glucometer (Lifespan, Milpitas, CA) on blood samples obtained from tail nicks at time points 15, 30, 60, 90, and 120 minutes after dextrose injection.

***Human tissue samples:*** Diaphragm specimens from human females were obtained from cadavers donated to the Anatomical Donation Program of the University of Michigan Medical School. Donors included one lean (BMI 22.0 kg/m$^2$) individual (72-years-old) and one individual with obesity (BMI 32.4 kg/m$^2$) (62-years-old)—neither with a medical history of congestive heart failure or primary pulmonary disease. Samples (approximately 4 x 4 cm) were obtained from the left costal diaphragm at the midpoint of the anterior-posterior axis, 2-3 cm medial to the rib attachment point. Samples were fixed for 48 hours in 4% paraformaldehyde at 4°C then paraffin embedded and sectioned (7$\mu$m thickness) in the transverse plane.

***Diaphragm Ultrasonography:*** Diaphragm ultrasonography was performed as previously described (71). Briefly, diaphragms were localized by ultrasound (US) using a transversely oriented MS250 transducer (frequency 24 MHz) (Visual Sonics, Toronto, ON). Diaphragm motion, observed in M-mode, was recorded for 3 or more respiratory cycles. Excursion amplitude, inspiratory and expiratory velocities were measured on still images with values averaged over the recorded cycles.

***Ex vivo isometric force testing (muscle strips):*** Isometric force testing on diaphragm strips was performed as previously described (27, 90). Briefly, tetanic force was measured on 2- to 4-mm-wide mid-costal diaphragm muscle strips. In a Krebs-Ringer bath containing 0.03 mmol/L tubocurarine chloride, held at 25°C and bubbled with 95% O2 and 5% CO2 (maintaining pH 7.4), an attached rib was sutured to a servomotor (model 305B; Aurora Scientific, Aurora, ON) and the free central tendon edge was sutured to a force transducer (model BG-50; Kulite Semiconductor Products, Leonia, NJ). A field generated between two platinum electrodes by a biphasic current stimulator (model 701A; Aurora Scientific) was employed to electrically stimulate the bath. LabVIEW 2014 software (National Instruments, Austin, TX) controlled the electrical pulse properties and servomotor activity while recording transducer data. Strips were adjusted to optimal length (Lo)—defined as the length at which a stimulus pulse elicited maximum isometric force (Po). Muscle cross-sectional area (CSA) was calculated using Lo and muscle mass. Specific force was calculated as the quotient of Po/CSA.

***Ex vivo isometric force testing (single myofibers):*** Single myofiber experiments were performed as previously described (91). Costal diaphragm fiber bundles (4mm in length and 1mm in diameter) containing longitudinal arrays of myofibers were manually excised from the central region of the muscle and then immediately immersed in ice-cold skinning solution [containing

potassium propionate, imidazole, and EGTA (Sigma)] for 30 minutes before storage at -80°C in a solution containing 50% glycerol by volume. Prior to each experiment, bundles were removed from storage and thawed before the removal of individual fibers by manual extraction with fine forceps under a stereomicroscope. Researchers were blinded to the experimental group when performing this testing.

Force responses and motor position were acquired through a 16-bit A-D board (NI-6052; National Instruments, Austin, TX) and analyzed on a computer running custom-designed LabVIEW software (National Instruments). The solution-changing system (model 802A; Aurora Scientific) consisted of three glass-bottom chambers housed in a moveable, temperature-controlled stainless-steel plate. Movement of the plate relative to the fiber was achieved via two stepper motors: one to lower and raise the chamber array and the other to translate the plate to a new chamber position.

Chamber 1 was filled with an EGTA-containing relaxing solution in which fibers could be manipulated. In this chamber, fibers were manually sutured to a servomotor (model 322; Aurora Scientific)-force transducer (model 403A; Aurora Scientific) apparatus with USP 10-0 monofilament nylon suture. Optimal sarcomere length was defined based on the diffraction pattern of laser light passed through the mounted fiber (92). Once achieved, the corresponding optimal fiber length (Lf) was measured under a stereomicroscope. Fiber CSA was estimated (on fibers held at Lf) using width and depth measurements obtained from high-magnification digital images of top and side views of the fiber. Chambers 2 and 3, respectively, contained a low-[Ca2+] pre-activating solution and a high-[$Ca2^{+}$] activating solution. Fibers were exposed to Chamber 2 solution for a 3-minute priming period during which the passive force required to maintain the fiber at Lf was measured. Fibers were then transferred to Chamber 3 to elicit maximum isometric force (Fo) during sustained contraction. Maximum total isometric force was calculated as the difference between Fo and passive force. Specific force was calculated as the quotient of maximum total isometric force/ CSA.

***Single-cell isolation:*** Diaphragmatic mononuclear cells were isolated through a protocol adapted from (28). Costal diaphragms were excised, minced with scissors, and digested in collagenase type II (Worthington Biochemical, Lakewood, NJ) diluted to 0.067% by weight in serum-free DMEM (ThermoFisher Scientific, Waltham, MA). After one 1-hour incubation at 37°C, samples were triturated 3-4 times through an 18-gauge needle, then incubated at 37°C for an additional 10 minutes. Next, collagenase was inactivated with an excess of DMEM containing 10% fetal bovine serum (FBS); samples were sequentially passed through 100 and 40 μm cell strainers to remove debris. Erythrocyte lysis was achieved via 30-second exposure to hypotonic stress, after which cells were re-suspended in phosphate-buffered saline (PBS).

Flow cytometry analysis used established marker profiles (28). Briefly, fresh cells were incubated in PBS with fluorophore-conjugated CD31, CD45, integrin α7, and Sca1 antibodies at dilutions indicated in (Supplementary Table 1) for 30 minutes at 4°C. DAPI was added for the final 5 minutes of the incubation to act as a dead cell marker. Cells were analyzed on a MoFlo Astrios EQ running Summit software (version 6.3; Beckman-Coulter, Brea, CA). Gates were established using fluorescence minus one approach; and plots were generated in FCS Express 7 (DeNovo Software).

***Cell Culture:*** After isolation, FAPs were cultured for 4 days in 12-well plates containing standard medium: DMEM with 10% FBS and antibiotic/antimycotic [penicillin, streptomycin, and amphotericin B (Sigma)]. Cells were then seeded at 30% confluence in optical bottom 96-well plates with standard medium and allowed to attach over 24 hours. The medium was then changed to DMEM with 1% FBS +/- THBS1 (5 μg/mL). After 3 days, cells were fixed, blocked, and immunostained as previously described (27) using antibody concentrations indicated in (Supplementary Table 1). For indicated experiments, SB-413542 (Millipore Sigma)—which impairs TGFβ receptor I and II-dependent signaling (93)—was added at 10 μg/mL, as previously

described (66), in parallel with THBS1. For BrdU (5-bromo-2'-deoxyuridine) staining, cells were incubated in 10μm BrdU (Abcam) for the 24 hours preceding analysis, then treated with 2M HCl (20 minutes at room temperature, following by 10 minutes at 37°C) to achieve DNA hydrolysis. For Ki67 staining, wash buffers and antibody diluents contained 0.2% Tween-20. Detergent was excluded for extracellular fibronectin staining. Counterstain with Alexa Fluor 488–conjugated phalloidin (Thermo Fisher Scientific) was used in specific experiments.

***Single-cell RNA sequencing and bioinformatics analysis:*** All mononuclear cell samples for scRNA-seq were isolated on the same day to obviate the need for batch effect correction. Sequencing was performed by the University of Michigan Advanced Genomics Core, with libraries constructed and subjected to 151 paired end cycles on the NovaSeq-6000 platform (Illumina, San Diego, CA). Bcl2fastq2 Conversion Software (Illumina) was used to generate de-multiplexed Fastq files. Mapping and quantitation were also done by the Advanced Genomics Core, using the ENSEMBL GRCm38 reference, and Cell Ranger to generate feature-barcode matrices, and aggregate the results from different samples. For all samples, Q30 bases in UMI were > 94%, reads mapped to the genome were > 94%, and fraction reads in cell were > 86%. Cell number in samples ranged from 3,774 to 4,369, while median UMI counts per cell ranged from 7,554 to 8,032. Approximately 10 million reads were sequenced per sample.

To produce velocity plots, velocyto (v. 0.17.17) and scVelo (v. 0.0.4, with Python 3.7.12) were used. Velocyto was installed as a conda environment. For each sample, the t-SNE coordinates were exported from the Loupe Browser with their barcode. Then velocyto was run from the command line with the t-SNE coordinates for each sample, a gtf file containing positions of repetitive elements to mask, the position-sorted bam file of filtered raw reads, and the mouse gtf file "Mus musculus.GRCm38.98.gtf". The output is a file in "Loom" format, designed to efficiently store single-cell datasets and metadata. The loom files were input to an R (v. 4.1.3) script with the package "reticulate" (v. 1.25), loaded to run Python in R. The Python package "scVelo" was

imported to the R script to calculate the cellular dynamics. For each sample, using the t-SNE coordinates and the calculated velocity, with ggplot2 (v 2.3.4) library loaded, a t-SNE plot could be produced with the rate and direction streams.

Using Loupe Browser 5, differential expression was calculated within FAP subclusters, and comparing each sample versus the two others combined. This gave a table of p-values and fold-changes that were uploaded to iPathwayGuide (advaitabio.com), using a linear absolute fold change cutoff of 1.5. All three comparisons in a subcluster were combined as a meta-analysis in iPathwayGuide, to visualize Venn diagrams of the marker genes and corresponding pathways.

***Whole tissue gene expression profiling:*** Costal hemidiaphragms were cleaned of adherent tissues, snap-frozen in liquid nitrogen, and digested in Trizol (ThermoFisher) with mechanical homogenization. Total RNA was isolated with RNeasy reagents (Qiagen, Germantown, MD) as per manufacturer's protocol. Samples were subjected to quality control via measurement of RIN values (TapeStation analysis software v3.2, Agilent Technologies). QuantSeq 3' mRNA sequencing (Lexogen, Vienna, Austria) was performed by the University of Michigan Advanced Genomics Core. Gene set enrichment analysis was performed using GSEA 4.1 software (University of California, San Diego). Volcano plots were generated in R Studio (Posit, PBC, Boston, MA). For quantitative PCR cDNA was synthesized with SuperScript II (Invitrogen, Carlsbad, CA), and the PCR reaction performed with SYBR Green (ThermoFisher) on a StepOnePlus machine (Applied Biosystems). Primer sequences for indicated genes (previously described in (27, 45)) are as follows: *Lep* forward: CAGTGCCTATCCAGAAAGTC; reverse: ATCTTGGACAAACTCAGAATG. *Pdgfra* forward: TTGATGAAGGTGGAACTGCT; reverse: ATTCCTCTGCCTGACATTGAC. *Fn1* forward: CGTTCATCTCCACTTGAT; reverse: CAGTTGTGTGCTCCGATCTC. *Col3a1* forward: CTTCTGGTTCTCCTGGTC; reverse: CAACCTTCACCCTTATCTCC. *Emr1* forward: CTTTGGCTATGGGCTTCCAGTC; reverse: GCAAGGAGGACAGAGTTTATCGTG.

***Histological Analysis:*** Seven μm-thick formalin-fixed, paraffin-embedded sections of the costal hemidiaphragm were prepared as previously described (27) and included samples in both transverse and longitudinal planes with respect to myofiber orientation. Both sample types were approximately 2-4 mm wide and included tissue encompassing the entire rib to tendon extent of the costal diaphragm muscle. Longitudinal samples were analyzed along the entire rib-tendon length, while transverse sections were analyzed at the midpoint of the rib-tendon axis. Hematoxylin/ eosin (H/E) and picrosirius red staining were performed by standard methods. Fiber size measurements were made using transverse sections stained with fluorescein 405-conjugated wheat germ agglutinin (WGA) (Biotium) diluted 1:200 in HBSS and incubated for 30 minutes at room temperature. Immunohistochemistry for perilipin, THY1 and fibronectin was performed with primary-secondary antibody pairs as indicated in (Supplementary Table 1). Staining of human tissue samples described above was performed using the same protocols and antibodies.

For myofiber typing analyses, excised costal diaphragm samples were sequentially submerged in 30% sucrose in PBS then a mixture of 30% sucrose in PBS/OCT (1:1) until the tissues no longer floated. Tissues were subsequently placed in an OCT solution and frozen in liquid nitrogen-cooled isopentane for cryosectioning. Seven μm-thick transverse cryosections were immunostained with two primary antibodies specifying type I and type IIa fibers (type IIb and type IIx fibers were unstained) as previously described (38). Primary and secondary antibodies are indicated in (Supplementary Table 1).

For immunofluorescent staining of CD68 and PDGFR$\alpha$, excised diaphragm tissues were directly embedded in OCT and quickly snap-frozen in liquid nitrogen-cooled isopentane. Seven μm-thick transverse or longitudinal cryosections (as described above) were fixed in 4% PFA/PBS for 5 min at room temperature, then blocked and permeabilized in 1% BSA/PBS or MOM blocking medium containing 0.5% Triton X-100. Tissue slides were stained with different combinations of

primary antibodies in 1% BSA/PBS or MOM antibody medium containing 0.1% Triton X-100 overnight at 4$^{o}$C, followed by corresponding secondary antibodies for 1 hour at room temperature. Primary-secondary antibody pairs are indicated in (Supplementary Table 1). Nuclei were counterstained with DAPI (diluted in deionized water) for 5 min at room temperature before mounting of samples Prolong Diamond (Invitrogen).

Samples were imaged using an Olympus DP72 camera mounted on an Olympus SZ61 microscope (Tokyo, Japan) or a Nikon A1 confocal microscope running NIS-Elements software (Olympus). For all forms of staining, at least 3 sections, separated from one another by at least 100 μm, were analyzed by individuals blinded to the experimental group; and quantitative morphometry was performed using NIH ImageJ.

***Statistics:*** Statistical analysis was performed in GraphPad Prism 10 and employed Student's two tailed t-test for two-group comparisons, one-way ANOVA (with Tukey post hoc test) or Kruksal-Wallis non-parametric test for comparisons of three or more groups, two-way ANOVA (with Sidak post hoc test) for two variables, and linear regression for correlation analysis. p value $<0.05$ indicated statistical significance. Quantitative data are shown as mean +/- SD.

***Study approval:*** The University of Michigan Institutional Animal Care and Use Committee (IACUC) approved all animal studies.

***Data availability:*** Sequencing data were made publicly available through upload to NCI Gene Expression Omnibus (GSE241005). Accession numbers are GSM7713701 (WT CD), GSM7713702 (WT HFD), and GSM7713703 (KO HFD). All other raw data values are provided in the Supporting Data Values file.

## AUTHOR CONTRIBUTIONS

E.D.B and T-H.C conceived of the study. E.D.B and T-H.C. designed the experiments with advice from D.R.C and S.V.B. E.D.B, M.S.W, R.K.V, S.H.K, C.S.D, and K.C.B performed the experiments. E.D.B and T-H.C analyzed the data with advice from S.V.B. E.D.B and T-H.C. wrote the manuscript; and D.E.M and S.V.B edited the manuscript.


## ACKNOWLEDGEMENTS

We thank the University of Michigan Advanced Genomics Core for single-cell and bulk RNA sequencing, the University of Michigan BCRF Bioinformatics Core for assistance with single-cell analyses, Dr. Jae-Eun Choi for assistance with bulk RNA sequencing analysis, and Dr. Helena Schotland for discussion on the clinical implications of our study. We acknowledge the Anatomical Donations Program of the University of Michigan Medical School (Dr. Glenn Fox) for providing human cadaveric diaphragm samples and specifically thank Mr. Clayne Frazer for his assistance with tissue harvest.

Research reported here was supported by the NHLBI (5 K08 HL14737701-05, to E.D.B.); NIDDK (R01DK095137 to T-H.C.); University of Michigan Bridging Fund, Biointerfaces Challenge Grant, and Michigan Integrative Musculoskeletal Health Core Center (MiMHC) P30 Center Pilot Feasibility Grant (to T-H.C); the Michigan Nutrition Obesity Research Center (MNORC) (AWD015548, to E.D.B.); and the Caswell Diabetes Institute (CDI) of the University of Michigan (F052716, to E.D.B.). The Michigan Musculoskeletal Health Center Function Core, in which ultrasound experiments were performed, is supported by NIAMS under award number P30 AR069620. The University of Michigan Animal Phenotyping Core, in which body composition testing was performed, is supported by awards U2CDK135066, DK020572, and DK089503.

## REFERENCES


1. Hales CM, Carroll MD, Fryar CD, and Ogden CL. Prevalence of Obesity and Severe Obesity Among Adults: United States, 2017-2018. *NCHS Data Brief.* 2020(360):1-8.
2. Gibson GJ. Obesity, respiratory function and breathlessness. *Thorax.* 2000;55 Suppl 1(Suppl 1):S41-4.
3. Babb TG, Ranasinghe KG, Comeau LA, Semon TL, and Schwartz B. Dyspnea on exertion in obese women: association with an increased oxygen cost of breathing. *Am J Respir Crit Care Med.* 2008;178(2):116-23.
4. Whipp BJ, and Davis JA. The ventilatory stress of exercise in obesity. *Am Rev Respir Dis.* 1984;129(2 Pt 2):S90-2.
5. Sin DD, Jones RL, and Man SF. Obesity is a risk factor for dyspnea but not for airflow obstruction. *Arch Intern Med.* 2002;162(13):1477-81.
6. Kessler R, Chaouat A, Schinkewitch P, Faller M, Casel S, Krieger J, et al. The obesity-hypoventilation syndrome revisited: a prospective study of 34 consecutive cases. *Chest.* 2001;120(2):369-76.
7. Mokhlesi B, Tulaimat A, Faibussowitsch I, Wang Y, and Evans AT. Obesity hypoventilation syndrome: prevalence and predictors in patients with obstructive sleep apnea. *Sleep Breath.* 2007;11(2):117-24.
8. Macavei VM, Spurling KJ, Loft J, and Makker HK. Diagnostic predictors of obesity-hypoventilation syndrome in patients suspected of having sleep disordered breathing. *J Clin Sleep Med.* 2013;9(9):879-84.
9. Laaban JP, and Chailleux E. Daytime hypercapnia in adult patients with obstructive sleep apnea syndrome in France, before initiating nocturnal nasal continuous positive airway pressure therapy. *Chest.* 2005;127(3):710-5.
10. Banerjee D, Yee BJ, Piper AJ, Zwillich CW, and Grunstein RR. Obesity hypoventilation syndrome: hypoxemia during continuous positive airway pressure. *Chest.* 2007;131(6):1678-84.
11. Lecube A, Sampol G, Lloberes P, Romero O, Mesa J, Morell F, et al. Asymptomatic sleep-disordered breathing in premenopausal women awaiting bariatric surgery. *Obes Surg.* 2010;20(4):454-61.
12. Bernhardt V, Stickford JL, Bhammar DM, and Babb TG. Aerobic exercise training without weight loss reduces dyspnea on exertion in obese women. *Respir Physiol Neurobiol.* 2016;221:64-70.
13. Bernhardt V, Bhammar DM, Marines-Price R, and Babb TG. Weight loss reduces dyspnea on exertion and unpleasantness of dyspnea in obese men. *Respir Physiol Neurobiol.* 2019;261:55-61.
14. Marines-Price R, Bernhardt V, Bhammar DM, and Babb TG. Dyspnea on exertion provokes unpleasantness and negative emotions in women with obesity. *Respir Physiol Neurobiol.* 2019;260:131-6.
15. Castro-Anon O, Perez de Llano LA, De la Fuente Sanchez S, Golpe R, Mendez Marote L, Castro-Castro J, et al. Obesity-hypoventilation syndrome: increased risk of death over sleep apnea syndrome. *PLoS One.* 2015;10(2):e0117808.
16. De Jong A, Chanques G, and Jaber S. Mechanical ventilation in obese ICU patients: from intubation to extubation. *Crit Care.* 2017;21(1):63.
17. Scano G, Stendardi L, and Bruni GI. The respiratory muscles in eucapnic obesity: their role in dyspnea. *Respir Med.* 2009;103(9):1276-85.
18. Cherniack RM, and Guenter CA. The efficiency of the respiratory muscles in obesity. *Can J Biochem Physiol.* 1961;39:1215-22.
19. Sahebjami H. Dyspnea in obese healthy men. *Chest.* 1998;114(5):1373-7.

20. Chlif M, Keochkerian D, Feki Y, Vaidie A, Choquet D, and Ahmaidi S. Inspiratory muscle activity during incremental exercise in obese men. *Int J Obes (Lond).* 2007;31(9):1456-63.
21. Lennmarken C, Sandstedt S, von Schenck H, and Larsson J. Skeletal muscle function and metabolism in obese women. *JPEN J Parenter Enteral Nutr.* 1986;10(6):583-7.
22. Newham DJ, Harrison RA, Tomkins AM, and Clark CG. The strength, contractile properties and radiological density of skeletal muscle before and 1 year after gastroplasty. *Clin Sci (Lond).* 1988;74(1):79-83.
23. Yu X, Huang YH, Feng YZ, Cheng ZY, Wang CC, and Cai XR. Association of Muscle Fat Content and Muscle Mass With Impaired Lung Function in Young Adults With Obesity: Evaluation With MRI. *Acad Radiol.* 2023.
24. Fadell EJ, Richman AD, Ward WW, and Hendon JR. Fatty infiltration of respiratory muscles in the Pick-wickian syndrome. *N Engl J Med.* 1962;266:861-3.
25. Popkin BM, Du S, Green WD, Beck MA, Algaith T, Herbst CH, et al. Individuals with obesity and COVID-19: A global perspective on the epidemiology and biological relationships. *Obes Rev.* 2020;21(11):e13128.
26. Shi Z, de Vries HJ, Vlaar APJ, van der Hoeven J, Boon RA, Heunks LMA, et al. Diaphragm Pathology in Critically Ill Patients With COVID-19 and Postmortem Findings From 3 Medical Centers. *JAMA Intern Med.* 2021;181(1):122-4.
27. Buras ED, Converso-Baran K, Davis CS, Akama T, Hikage F, Michele DE, et al. Fibro-Adipogenic Remodeling of the Diaphragm in Obesity-Associated Respiratory Dysfunction. *Diabetes.* 2019;68(1):45-56.
28. Joe AW, Yi L, Natarajan A, Le Grand F, So L, Wang J, et al. Muscle injury activates resident fibro/adipogenic progenitors that facilitate myogenesis. *Nat Cell Biol.* 2010;12(2):153-63.
29. Uezumi A, Fukada S, Yamamoto N, Takeda S, and Tsuchida K. Mesenchymal progenitors distinct from satellite cells contribute to ectopic fat cell formation in skeletal muscle. *Nat Cell Biol.* 2010;12(2):143-52.
30. Uezumi A, Fukada S, Yamamoto N, Ikemoto-Uezumi M, Nakatani M, Morita M, et al. Identification and characterization of PDGFRalpha+ mesenchymal progenitors in human skeletal muscle. *Cell Death Dis.* 2014;5(4):e1186.
31. Heredia JE, Mukundan L, Chen FM, Mueller AA, Deo RC, Locksley RM, et al. Type 2 innate signals stimulate fibro/adipogenic progenitors to facilitate muscle regeneration. *Cell.* 2013;153(2):376-88.
32. Lemos DR, Babaeijandaghi F, Low M, Chang CK, Lee ST, Fiore D, et al. Nilotinib reduces muscle fibrosis in chronic muscle injury by promoting TNF-mediated apoptosis of fibro/adipogenic progenitors. *Nat Med.* 2015;21(7):786-94.
33. Wosczyna MN, Konishi CT, Perez Carbajal EE, Wang TT, Walsh RA, Gan Q, et al. Mesenchymal Stromal Cells Are Required for Regeneration and Homeostatic Maintenance of Skeletal Muscle. *Cell Rep.* 2019;27(7):2029-35 e5.
34. Madaro L, Passafaro M, Sala D, Etxaniz U, Lugarini F, Proietti D, et al. Denervation-activated STAT3-IL-6 signalling in fibro-adipogenic progenitors promotes myofibres atrophy and fibrosis. *Nat Cell Biol.* 2018;20(8):917-27.
35. Uezumi A, Ito T, Morikawa D, Shimizu N, Yoneda T, Segawa M, et al. Fibrosis and adipogenesis originate from a common mesenchymal progenitor in skeletal muscle. *J Cell Sci.* 2011;124(Pt 21):3654-64.
36. Mozzetta C, Consalvi S, Saccone V, Tierney M, Diamantini A, Mitchell KJ, et al. Fibroadipogenic progenitors mediate the ability of HDAC inhibitors to promote regeneration in dystrophic muscles of young, but not old Mdx mice. *EMBO Mol Med.* 2013;5(4):626-39.

37. Larouche JA, Wallace EC, Spence BD, Buras E, and Aguilar CA. Spatiotemporal mapping of immune and stem cell dysregulation after volumetric muscle loss. *JCI Insight.* 2023.
38. Biltz NK, Collins KH, Shen KC, Schwartz K, Harris CA, and Meyer GA. Infiltration of intramuscular adipose tissue impairs skeletal muscle contraction. *J Physiol.* 2020;598(13):2669-83.
39. McKellar DW, Walter LD, Song LT, Mantri M, Wang MFZ, De Vlaminck I, et al. Large-scale integration of single-cell transcriptomic data captures transitional progenitor states in mouse skeletal muscle regeneration. *Commun Biol.* 2021;4(1):1280.
40. Farup J, Just J, de Paoli F, Lin L, Jensen JB, Billeskov T, et al. Human skeletal muscle CD90(+) fibro-adipogenic progenitors are associated with muscle degeneration in type 2 diabetic patients. *Cell Metab.* 2021;33(11):2201-14 e11.
41. Varma V, Yao-Borengasser A, Bodles AM, Rasouli N, Phanavanh B, Nolen GT, et al. Thrombospondin-1 is an adipokine associated with obesity, adipose inflammation, and insulin resistance. *Diabetes.* 2008;57(2):432-9.
42. Ramis JM, Franssen-van Hal NL, Kramer E, Llado I, Bouillaud F, Palou A, et al. Carboxypeptidase E and thrombospondin-1 are differently expressed in subcutaneous and visceral fat of obese subjects. *Cell Mol Life Sci.* 2002;59(11):1960-71.
43. Kong P, Gonzalez-Quesada C, Li N, Cavalera M, Lee DW, and Frangogiannis NG. Thrombospondin-1 regulates adiposity and metabolic dysfunction in diet-induced obesity enhancing adipose inflammation and stimulating adipocyte proliferation. *Am J Physiol Endocrinol Metab.* 2013;305(3):E439-50.
44. Matsuo Y, Tanaka M, Yamakage H, Sasaki Y, Muranaka K, Hata H, et al. Thrombospondin 1 as a novel biological marker of obesity and metabolic syndrome. *Metabolism.* 2015;64(11):1490-9.
45. Inoue M, Jiang Y, Barnes RH, 2nd, Tokunaga M, Martinez-Santibanez G, Geletka L, et al. Thrombospondin 1 mediates high-fat diet-induced muscle fibrosis and insulin resistance in male mice. *Endocrinology.* 2013;154(12):4548-59.
46. Belotti D, Capelli C, Resovi A, Introna M, and Taraboletti G. Thrombospondin-1 promotes mesenchymal stromal cell functions via TGFbeta and in cooperation with PDGF. *Matrix Biol.* 2016;55:106-16.
47. De Luna N, Gallardo E, Sonnet C, Chazaud B, Dominguez-Perles R, Suarez-Calvet X, et al. Role of thrombospondin 1 in macrophage inflammation in dysferlin myopathy. *J Neuropathol Exp Neurol.* 2010;69(6):643-53.
48. Suarez-Calvet X, Alonso-Perez J, Castellvi I, Carrasco-Rozas A, Fernandez-Simon E, Zamora C, et al. Thrombospondin-1 mediates muscle damage in brachio-cervical inflammatory myopathy and systemic sclerosis. *Neurol Neuroimmunol Neuroinflamm.* 2020;7(3).
49. Malecova B, Gatto S, Etxaniz U, Passafaro M, Cortez A, Nicoletti C, et al. Dynamics of cellular states of fibro-adipogenic progenitors during myogenesis and muscular dystrophy. *Nat Commun.* 2018;9(1):3670.
50. Giuliani G, Rosina M, and Reggio A. Signaling pathways regulating the fate of fibro/adipogenic progenitors (FAPs) in skeletal muscle regeneration and disease. *FEBS J.* 2022;289(21):6484-517.
51. Rubenstein AB, Smith GR, Raue U, Begue G, Minchev K, Ruf-Zamojski F, et al. Single-cell transcriptional profiles in human skeletal muscle. *Sci Rep.* 2020;10(1):229.
52. Oprescu SN, Yue F, Qiu J, Brito LF, and Kuang S. Temporal Dynamics and Heterogeneity of Cell Populations during Skeletal Muscle Regeneration. *iScience.* 2020;23(4):100993.
53. Saleh KK, Xi H, Switzler C, Skuratovsky E, Romero MA, Chien P, et al. Single cell sequencing maps skeletal muscle cellular diversity as disease severity increases in dystrophic mouse models. *iScience.* 2022;25(11):105415.

54. Hepler C, Shan B, Zhang Q, Henry GH, Shao M, Vishvanath L, et al. Identification of functionally distinct fibro-inflammatory and adipogenic stromal subpopulations in visceral adipose tissue of adult mice. *Elife.* 2018;7.
55. Fitzgerald G, Turiel G, Gorski T, Soro-Arnaiz I, Zhang J, Casartelli NC, et al. MME(+) fibro-adipogenic progenitors are the dominant adipogenic population during fatty infiltration in human skeletal muscle. *Commun Biol.* 2023;6(1):111.
56. Merrick D, Sakers A, Irgebay Z, Okada C, Calvert C, Morley MP, et al. Identification of a mesenchymal progenitor cell hierarchy in adipose tissue. *Science.* 2019;364(6438).
57. Petrus P, Fernandez TL, Kwon MM, Huang JL, Lei V, Safikhan NS, et al. Specific loss of adipocyte CD248 improves metabolic health via reduced white adipose tissue hypoxia, fibrosis and inflammation. *EBioMedicine.* 2019;44:489-501.
58. Egea V, Zahler S, Rieth N, Neth P, Popp T, Kehe K, et al. Tissue inhibitor of metalloproteinase-1 (TIMP-1) regulates mesenchymal stem cells through let-7f microRNA and Wnt/beta-catenin signaling. *Proc Natl Acad Sci U S A.* 2012;109(6):E309-16.
59. Lee EJ, Jan AT, Baig MH, Ashraf JM, Nahm SS, Kim YW, et al. Fibromodulin: a master regulator of myostatin controlling progression of satellite cells through a myogenic program. *FASEB J.* 2016;30(8):2708-19.
60. Descamps S, Arzouk H, Bacou F, Bernardi H, Fedon Y, Gay S, et al. Inhibition of myoblast differentiation by Sfrp1 and Sfrp2. *Cell Tissue Res.* 2008;332(2):299-306.
61. Giordani L, He GJ, Negroni E, Sakai H, Law JYC, Siu MM, et al. High-Dimensional Single-Cell Cartography Reveals Novel Skeletal Muscle-Resident Cell Populations. *Mol Cell.* 2019;74(3):609-21 e6.
62. Docheva D, Hunziker EB, Fassler R, and Brandau O. Tenomodulin is necessary for tenocyte proliferation and tendon maturation. *Mol Cell Biol.* 2005;25(2):699-705.
63. Yao L, Conforti F, Hill C, Bell J, Drawater L, Li J, et al. Paracrine signalling during ZEB1-mediated epithelial-mesenchymal transition augments local myofibroblast differentiation in lung fibrosis. *Cell Death Differ.* 2019;26(5):943-57.
64. Meng Q, Bhandary B, Bhuiyan MS, James J, Osinska H, Valiente-Alandi I, et al. Myofibroblast-Specific TGFbeta Receptor II Signaling in the Fibrotic Response to Cardiac Myosin Binding Protein C-Induced Cardiomyopathy. *Circ Res.* 2018;123(12):1285-97.
65. Qadri M, Jay GD, Zhang LX, Richendrfer H, Schmidt TA, and Elsaid KA. Proteoglycan-4 regulates fibroblast to myofibroblast transition and expression of fibrotic genes in the synovium. *Arthritis Res Ther.* 2020;22(1):113.
66. Halder SK, Beauchamp RD, and Datta PK. A specific inhibitor of TGF-beta receptor kinase, SB-431542, as a potent antitumor agent for human cancers. *Neoplasia.* 2005;7(5):509-21.
67. Lerbs T, Cui L, King ME, Chai T, Muscat C, Chung L, et al. CD47 prevents the elimination of diseased fibroblasts in scleroderma. *JCI Insight.* 2020;5(16).
68. Dawson DW, Pearce SF, Zhong R, Silverstein RL, Frazier WA, and Bouck NP. CD36 mediates the In vitro inhibitory effects of thrombospondin-1 on endothelial cells. *J Cell Biol.* 1997;138(3):707-17.
69. Yadav H, Quijano C, Kamaraju AK, Gavrilova O, Malek R, Chen W, et al. Protection from obesity and diabetes by blockade of TGF-beta/Smad3 signaling. *Cell Metab.* 2011;14(1):67-79.
70. Jaitin DA, Adlung L, Thaiss CA, Weiner A, Li B, Descamps H, et al. Lipid-Associated Macrophages Control Metabolic Homeostasis in a Trem2-Dependent Manner. *Cell.* 2019;178(3):686-98 e14.
71. Whitehead NP, Bible KL, Kim MJ, Odom GL, Adams ME, and Froehner SC. Validation of ultrasonography for non-invasive assessment of diaphragm function in muscular dystrophy. *J Physiol.* 2016;594(24):7215-27.

72. McLaren KM. Immunohistochemical localisation of thrombospondin in human megakaryocytes and platelets. *J Clin Pathol.* 1983;36(2):197-9.
73. Jaffe EA, Ruggiero JT, Leung LK, Doyle MJ, McKeown-Longo PJ, and Mosher DF. Cultured human fibroblasts synthesize and secrete thrombospondin and incorporate it into extracellular matrix. *Proc Natl Acad Sci U S A.* 1983;80(4):998-1002.
74. Mosher DF, Doyle MJ, and Jaffe EA. Synthesis and secretion of thrombospondin by cultured human endothelial cells. *J Cell Biol.* 1982;93(2):343-8.
75. Isenberg JS, and Roberts DD. Thrombospondin-1 in maladaptive aging responses: a concept whose time has come. *Am J Physiol Cell Physiol.* 2020;319(1):C45-C63.
76. von Toerne C, Huth C, de Las Heras Gala T, Kronenberg F, Herder C, Koenig W, et al. MASP1, THBS1, GPLD1 and ApoA-IV are novel biomarkers associated with prediabetes: the KORA F4 study. *Diabetologia.* 2016;59(9):1882-92.
77. Bohm A, Hoffmann C, Irmler M, Schneeweiss P, Schnauder G, Sailer C, et al. TGF-beta Contributes to Impaired Exercise Response by Suppression of Mitochondrial Key Regulators in Skeletal Muscle. *Diabetes.* 2016;65(10):2849-61.
78. Saito Y, Chikenji TS, Matsumura T, Nakano M, and Fujimiya M. Exercise enhances skeletal muscle regeneration by promoting senescence in fibro-adipogenic progenitors. *Nat Commun.* 2020;11(1):889.
79. Murphy-Ullrich JE. Thrombospondin 1 and Its Diverse Roles as a Regulator of Extracellular Matrix in Fibrotic Disease. *J Histochem Cytochem.* 2019;67(9):683-99.
80. Hocevar BA, Brown TL, and Howe PH. TGF-beta induces fibronectin synthesis through a c-Jun N-terminal kinase-dependent, Smad4-independent pathway. *EMBO J.* 1999;18(5):1345-56.
81. Salimena MC, Lagrota-Candido J, and Quirico-Santos T. Gender dimorphism influences extracellular matrix expression and regeneration of muscular tissue in mdx dystrophic mice. *Histochem Cell Biol.* 2004;122(5):435-44.
82. Potluri T, Taylor MJ, Stulberg JJ, Lieber RL, Zhao H, and Bulun SE. An estrogen-sensitive fibroblast population drives abdominal muscle fibrosis in an inguinal hernia mouse model. *JCI Insight.* 2022;7(9).
83. Hausman GJ, Basu U, Du M, Fernyhough-Culver M, and Dodson MV. Intermuscular and intramuscular adipose tissues: Bad vs. good adipose tissues. *Adipocyte.* 2014;3(4):242-55.
84. Claflin DR, and Brooks SV. Direct observation of failing fibers in muscles of dystrophic mice provides mechanistic insight into muscular dystrophy. *Am J Physiol Cell Physiol.* 2008;294(2):C651-8.
85. Roche SM, Gumucio JP, Brooks SV, Mendias CL, and Claflin DR. Measurement of Maximum Isometric Force Generated by Permeabilized Skeletal Muscle Fibers. *J Vis Exp.* 2015(100):e52695.
86. Pellegrinelli V, Rouault C, Rodriguez-Cuenca S, Albert V, Edom-Vovard F, Vidal-Puig A, et al. Human Adipocytes Induce Inflammation and Atrophy in Muscle Cells During Obesity. *Diabetes.* 2015;64(9):3121-34.
87. Orwoll ES, Blackwell T, Cummings SR, Cauley JA, Lane NE, Hoffman AR, et al. CT Muscle Density, D3Cr Muscle Mass, and Body Fat Associations With Physical Performance, Mobility Outcomes, and Mortality Risk in Older Men. *J Gerontol A Biol Sci Med Sci.* 2022;77(4):790-9.
88. Jiang N, Zhang Z, Shao X, Jing R, Wang C, Fang W, et al. Blockade of thrombospondin-1 ameliorates high glucose-induced peritoneal fibrosis through downregulation of TGF-beta1/Smad3 signaling pathway. *J Cell Physiol.* 2020;235(1):364-79.
89. Lu A, Miao M, Schoeb TR, Agarwal A, and Murphy-Ullrich JE. Blockade of TSP1-dependent TGF-beta activity reduces renal injury and proteinuria in a murine model of diabetic nephropathy. *Am J Pathol.* 2011;178(6):2573-86.

90. Brooks SV, and Faulkner JA. Contractile properties of skeletal muscles from young, adult and aged mice. *J Physiol.* 1988;404:71-82.
91. Larkin LM, Hanes MC, Kayupov E, Claflin DR, Faulkner JA, and Brooks SV. Weakness of whole muscles in mice deficient in Cu, Zn superoxide dismutase is not explained by defects at the level of the contractile apparatus. *Age (Dordr).* 2013;35(4):1173-81.
92. Mendias CL, Kayupov E, Bradley JR, Brooks SV, and Claflin DR. Decreased specific force and power production of muscle fibers from myostatin-deficient mice are associated with a suppression of protein degradation. *J Appl Physiol (1985).* 2011;111(1):185-91.
93. Goumans MJ, Liu Z, and ten Dijke P. TGF-beta signaling in vascular biology and dysfunction. *Cell Res.* 2009;19(1):116-27.

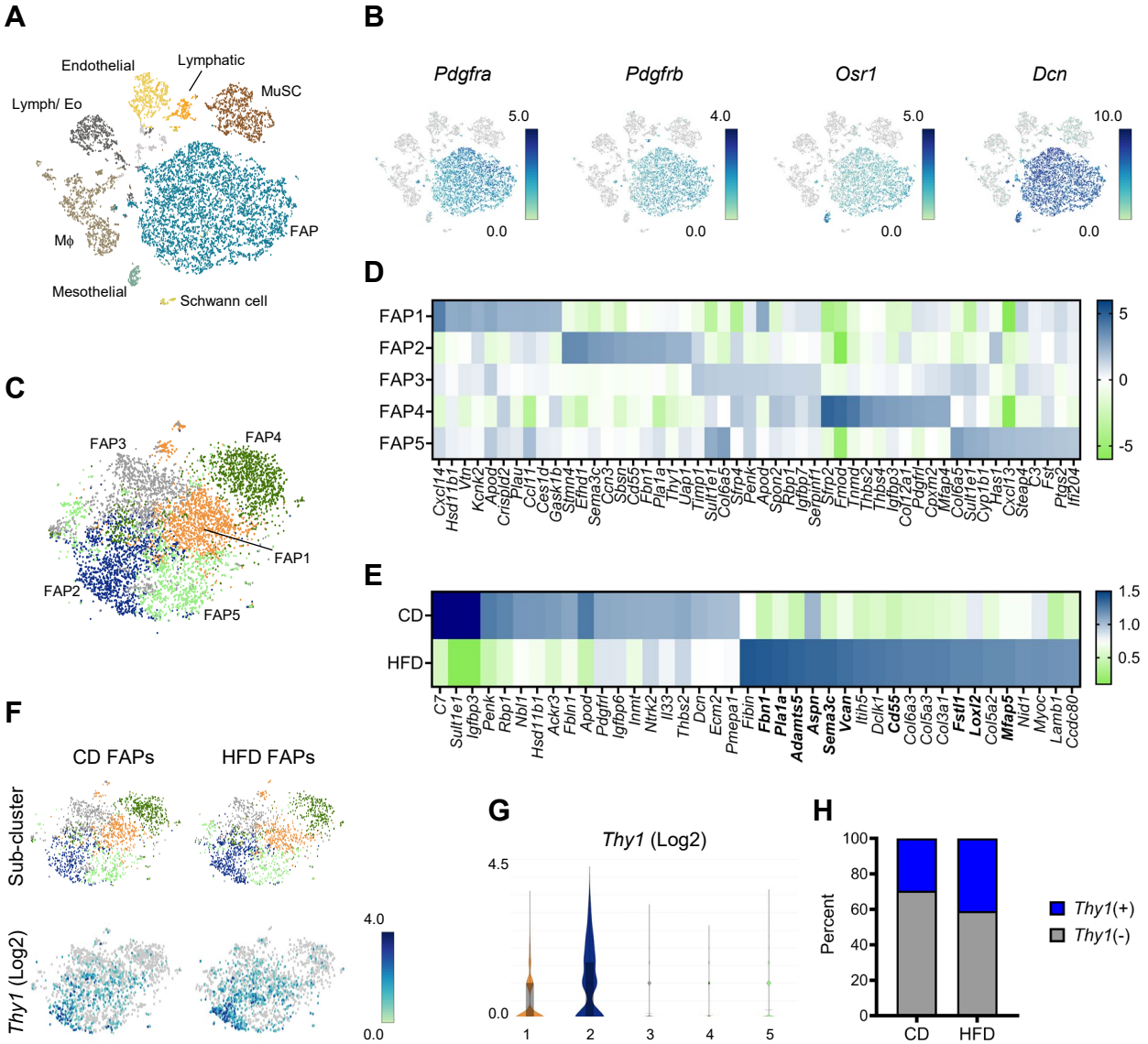


**Figure 1. The diaphragm FAP population is heterogeneous and altered by obesity. (A)** tSNE plot: Mononuclear cells from pooled diaphragms of 6-month high-fat diet (HFD)-fed and age-matched control diet (CD)-fed male C57Bl/6J mice n= 2 mice per group. **(B)** tSNE plots: FAP marker genes. **(C)** tSNE plots: FAP sub-populations from pooled CD and HFD samples. **(D)** Heat map showing transcripts enriched in FAP sub-clusters. **(E)** Heat map showing genes enriched in total FAP populations from CD and HFD samples. Bolded gene names are enriched in the FAP2 sub-cluster. **(F)** tSNE and violin plots showing FAP sub-clusters and *Thy1* expression in CD and HFD samples. **(G)** Violin plots indicating cluster-specific *Thy1* expression. **(H)** Percentage of *Thy1*-expressing among FAPs from CD and HFD samples.

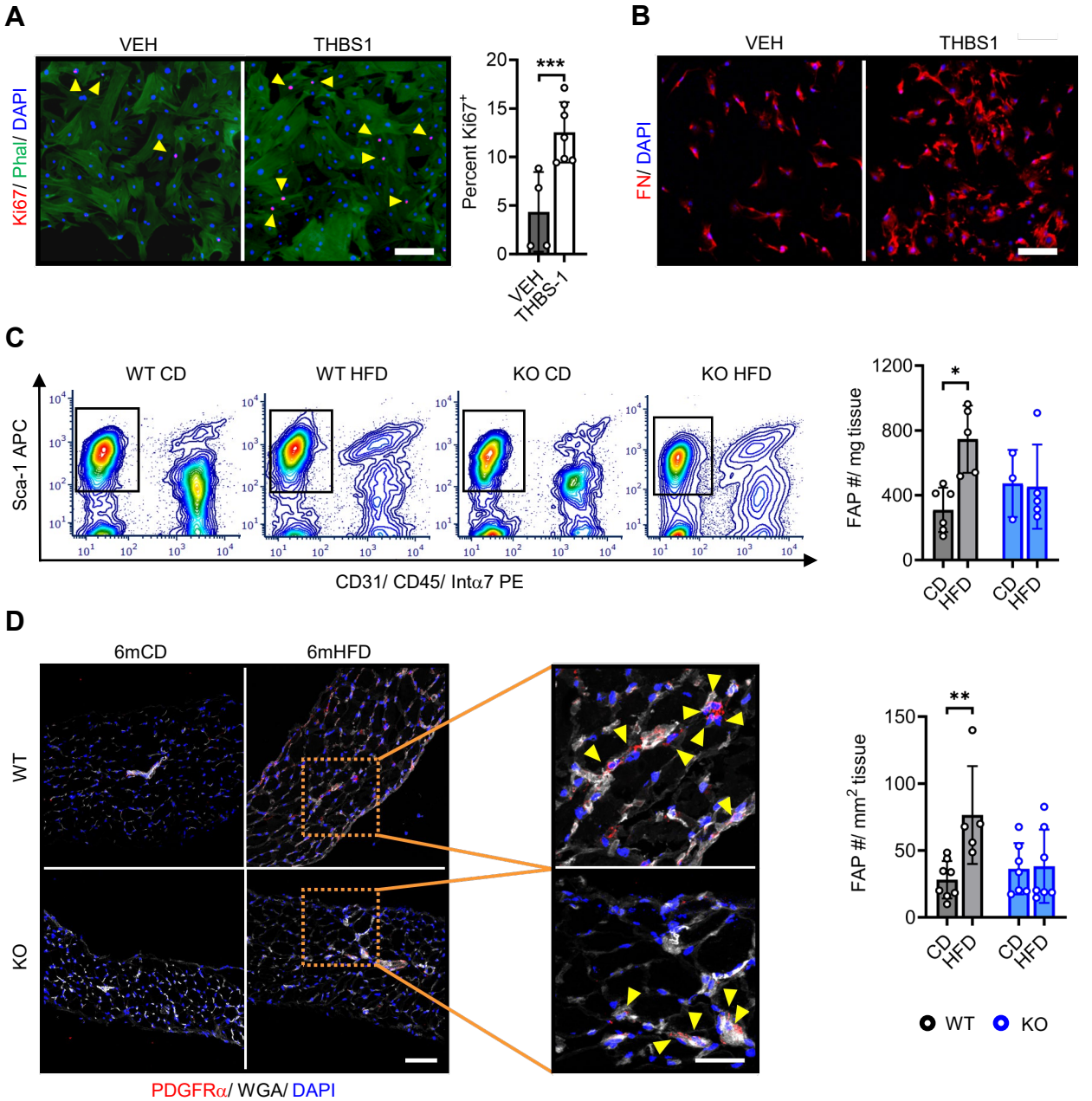


**Figure 2. HFD-feeding causes THBS1-dependent FAP population expansion. (A)** Primary FACS-isolated FAPs treated with THBS1 (5μg/mL) or DMEM vehicle (VEH) and subjected to Ki67 immunocytochemistry with phalloidin (PHAL) counterstain. Scale 50 μm. The bar graph indicates percent Ki67⁺ cells. n= 2 unique experiments per group with 4-7 replicates per experiment. **(B)** Primary FAPs treated as indicated in (A) and subjected to fibronectin (FN) immunocytochemistry. Representative images from 2 unique experiments with 3-4 replicates per experiment. Scale 50 μm. **(C)** Analysis of FAPs from costal diaphragm tissue of wild type (WT) and *Thbs1*$^{-/-}$ (KO) mice fed a control diet (CD) or high-fat diet (HFD) for 6 months. Left panels show representative flow cytometry plots—FAPs are positive for Sca-1 and negative for CD31, CD45, and integrin α7 (Intα7). Right panel shows bar graph quantifying FAPs per mg tissue. Each sample contains 2 whole costal diaphragms. n= 3-6 samples (6-12 mice) per group. **(D)** Immunohistochemistry for PDGFRα, with wheat germ agglutin (WGA) counterstain, in diaphragm samples from WT and KO mice fed CD or HFD for 6 months. Scale 100 μm in main panel, 50 μm in inset. Arrowheads in insert indicate FAPs, defined as PDGFRα staining surrounding a DAPI⁺ nucleus. Bar graph indicates the quantification of PDGFRα⁺ cells/ mm$^2$ tissue cross-sectional area (CSA). n= 5-8 mice per group. Statistical analysis with t-test for individual comparisons, two-way ANOVA for multiple variable comparisons. Error bars indicate SDM. *p<0.05, **p<0.01, ***p<0.001.

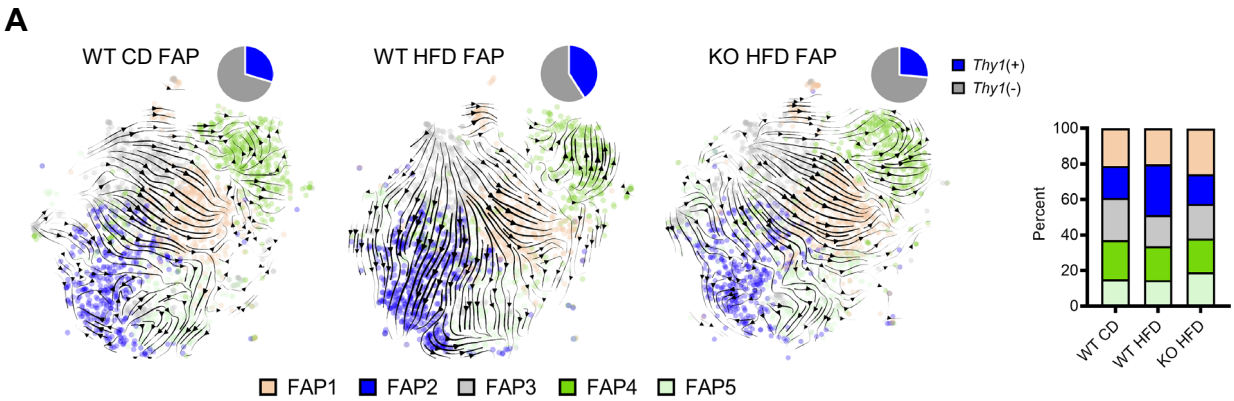


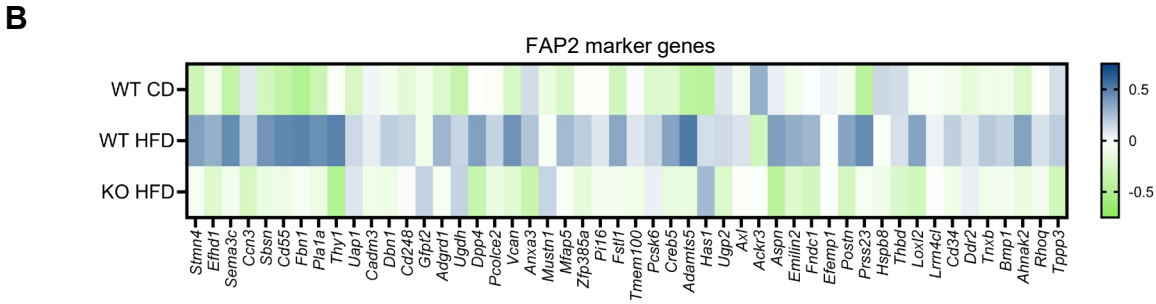


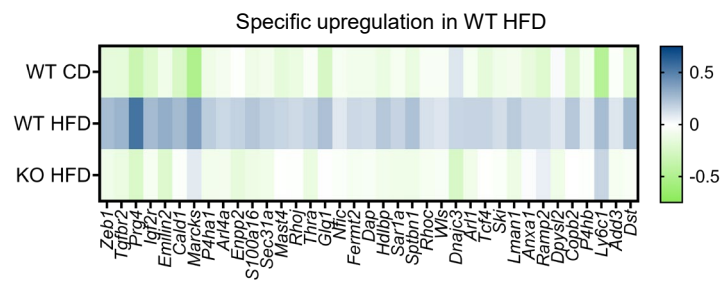


**D**

| WT HFD-enriched biological processes | P-val (corr) |
|---|---|
| TGFβ receptor signaling pathway | 0.0200 |
| Cellular response to amino acid stimulus | 0.0260 |
| Positive regulation of biological process | 0.0280 |
| Response to endogenous stimulus | 0.0280 |
| Cellular response to TGFβ stimulus | 0.0300 |
| Cartilage devel involved in endochon bone morph | 0.0310 |
| Endocardial cushion development | 0.0310 |
| Negative regulation of developmental process | 0.0310 |
| Response to TGFβ | 0.0360 |
| Gland morphogenesis | 0.0360 |
| Regulation of anatomical structure morphogenesis | 0.0390 |
| Gland development | 0.0400 |
| Regulation of TGFβ receptor signaling pathway | 0.0400 |
| Regulation of cellular response to TGFβ stimulus | 0.0400 |
| Vascular process in circulatory system | 0.0400 |
| Cell morphogenesis | 0.0440 |
| Pattern specification process | 0.0440 |
| Neurogenesis | 0.0450 |

**Figure 3. *Thbs1* is required for obesity-induced FAP sub-population shifts. (A)** Velocity plots demonstrating temporal relationships between FAP sub-populations in wild-type (WT) mice fed CD or HFD for 6 months; and *Thbs1*$^{-/-}$ (KO) mice fed HFD for 6 months. Arrow directions represent the trajectory of differentiation between sub-populations. Thickness of arrow indicates a rate of change. Pie charts indicate percentage of *Thy1*-expressing cells in each group. Stacked bar graph shows proportion of individual FAP sub-populations in each group. n= 2 mice per group. **(B)** Heat map indicating the expression of FAP2 marker genes in each group. **(C)** Heat map showing genes specifically enriched in the WT HFD group. **(D)** Gene ontology terms (Biological Processes) specifically enriched in WT HFD FAPs, with corrected p-values.

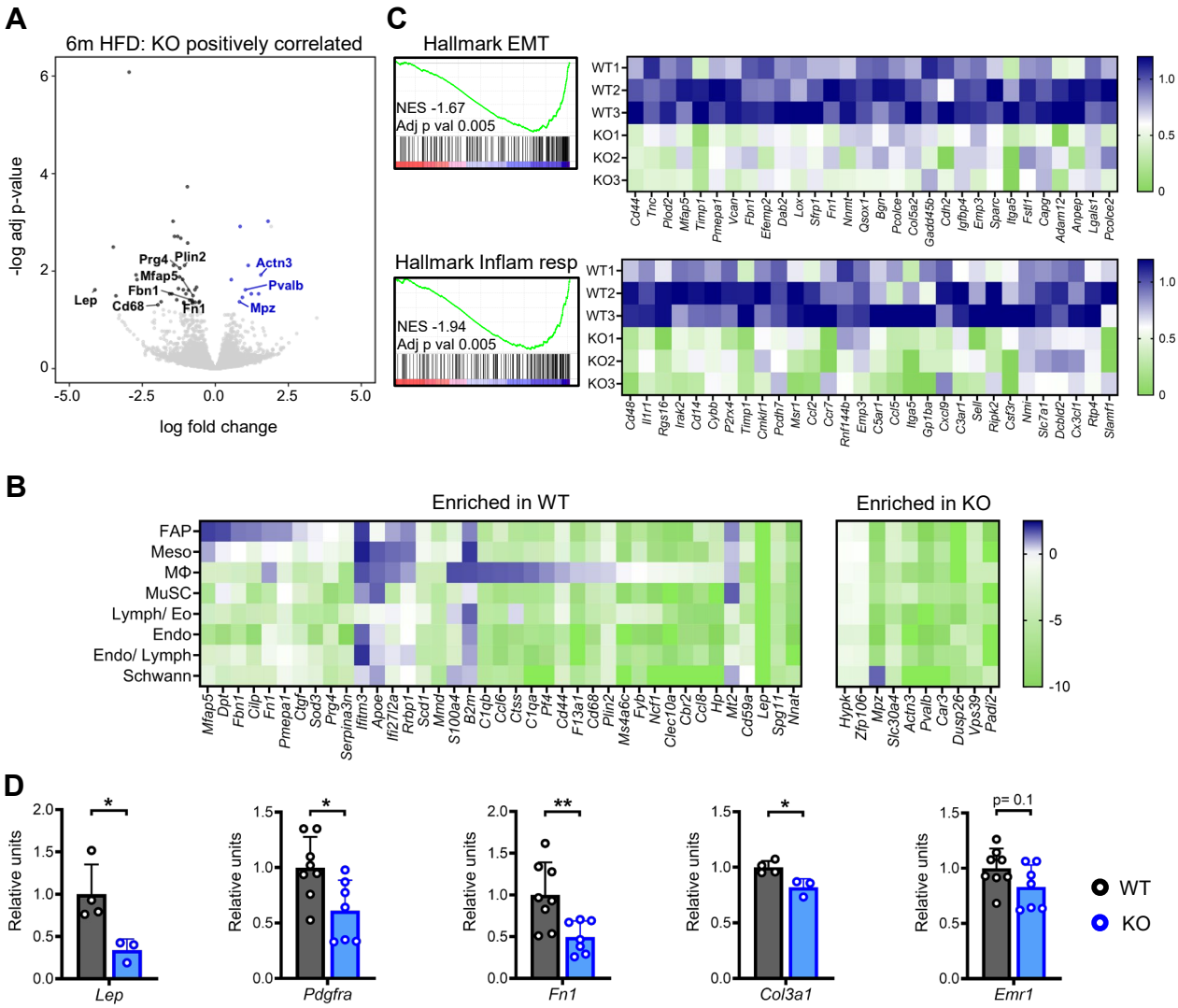


**Figure 4. Whole tissue transcriptomics highlights enrichment of stromal genes in wild type versus *Thbs1*$^{-/-}$ mice subjected to DIO. (A)** Volcano plot of whole costal diaphragm RNA-seq demonstrating differentially expressed genes between wild-type (WT) and *Thbs1*$^{-/-}$ (KO) mice fed high-fat diet (HFD) for 6 months (6m HFD). n= 3 mice per group. x-axis indicates log fold change (FC) in KO versus WT. y-axis indicates -log adjusted p-value. **(B)** Heat map integrating tissue-level RNA-seq with scRNA-seq data. Genes indicated are those enriched in WT and KO mice on bulk RNA sequencing [i.e., the points on the volcano plot in (A)]. Cell types are those identified on scRNA-seq (as shown in Fig 1A). Heat maps show cell-type specific expression as defined on scRNA-seq. **(C)** Enrichment plots demonstrating selected HALLMARK pathways differentially expressed between 6m HFD-fed WT and KO mice: EPITHELIAL MESENCHYMAL TRANSITION (Hallmark EMT) and INFLAMMATORY RESPONSE (Hallmark Inflamm resp). Heat maps show the expression of leading-edge genes in individual samples. **(D)** QPCR analysis of selected genes performed on costal diaphragm tissue of 6m HFD WT and 6m HFD KO mice. n= 3-8 whole hemidiaphragm samples per group. Statistical analysis with t-test. Error bars indicate SDM. *p<0.05, **p<0.01.

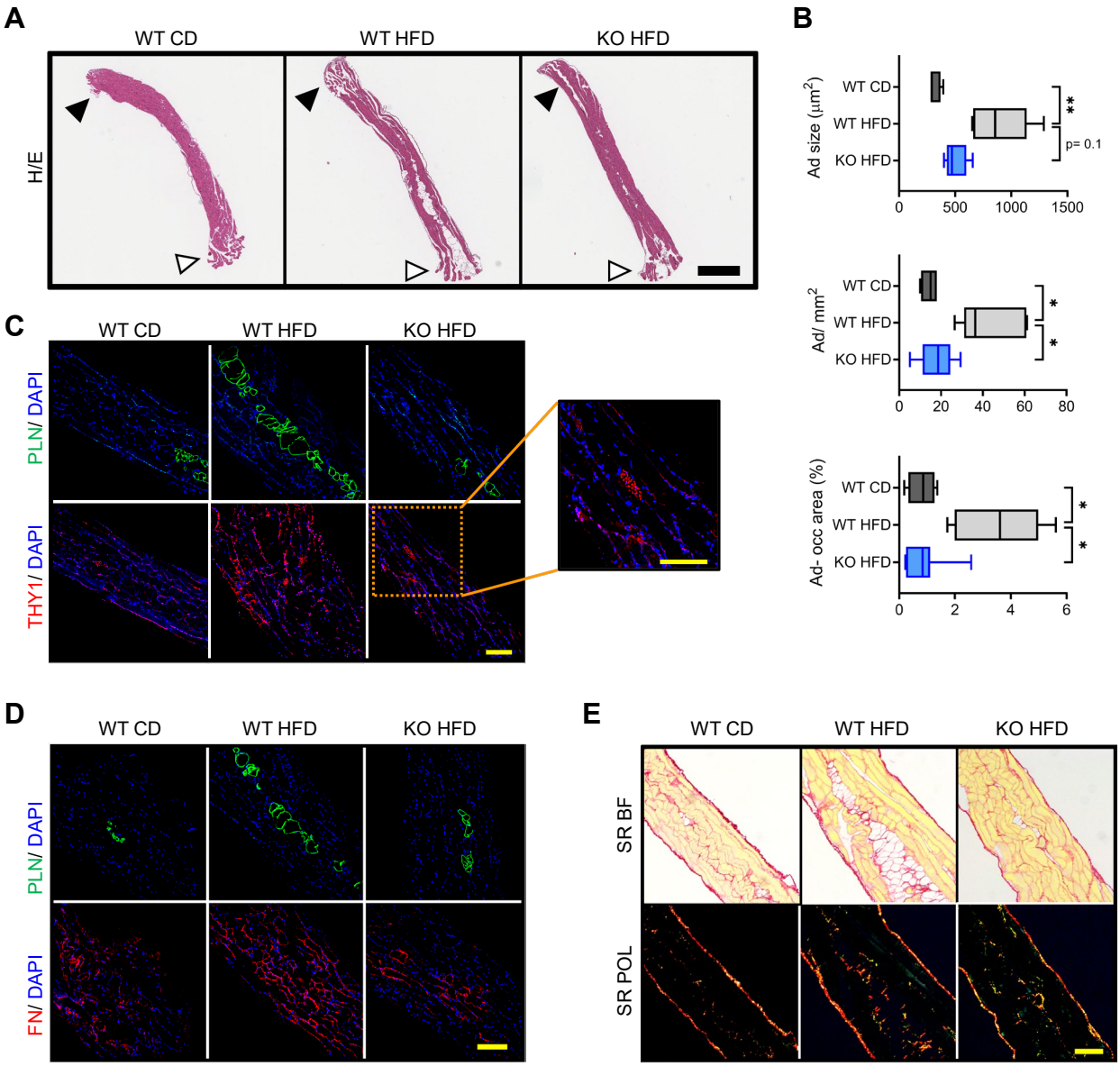


**Figure 5. *Thbs1* ablation protects against diaphragm fibro-adipogenic remodeling. (A)** H/E-stained longitudinal diaphragm sections from wild-type mice fed control diet (WT CD) or HFD (WT HFD) for 6 months; and *Thbs1*$^{-/-}$ (KO) mice fed HFD for 6 months (KO HFD). White arrowhead indicates rib attachment point. Black arrowhead indicates central tendon attachment point. Scale 600 μm. Representative samples from 5-7 mice per group. **(B)** Adipocyte size, adipocyte number per mm cross-sectional area, and percent total cross-sectional area occupied by adipocytes in samples described in (A). Values are the average of measurements made on 3 non-consecutive 7 μm-thick sections encompassing the entire rib-to-tendon extent of muscle. n= 4-7 mice per group. Box indicates 25$^{th}$-75$^{th}$ percentile, midline indicates median, whiskers indicate minimum and maximum values. **(C)** Immunofluorescent staining of perilipin (PLN) and THY1 on adjacent 7 μm-thick longitudinal sections from animals described above. Representative images from analysis of 5-7 mice per group. Inset indicates THY1 staining of a nerve passing through the sample, representing an internal positive staining control. Scale 200 μm. **(D)** PLN and fibronectin (FN) staining on adjacent 7 μm-thick longitudinal sections from animals described above. Representative images from analysis of 5-7 mice per group. Scale 200 um. **(E)** Picrosirius red (SR) staining of 7 μm-thick longitudinal sections from animals described above. Bright-field (BF) and polarized light (POL) images: polymerized collagens fluoresce red/ yellow under polarized light. Representative images from analysis of 5-7 mice per group. Scale 200 μm. Statistical analysis with Kruksal-Wallis test for non-parametric multiple comparisons. *p<0.05, **p,0.01.

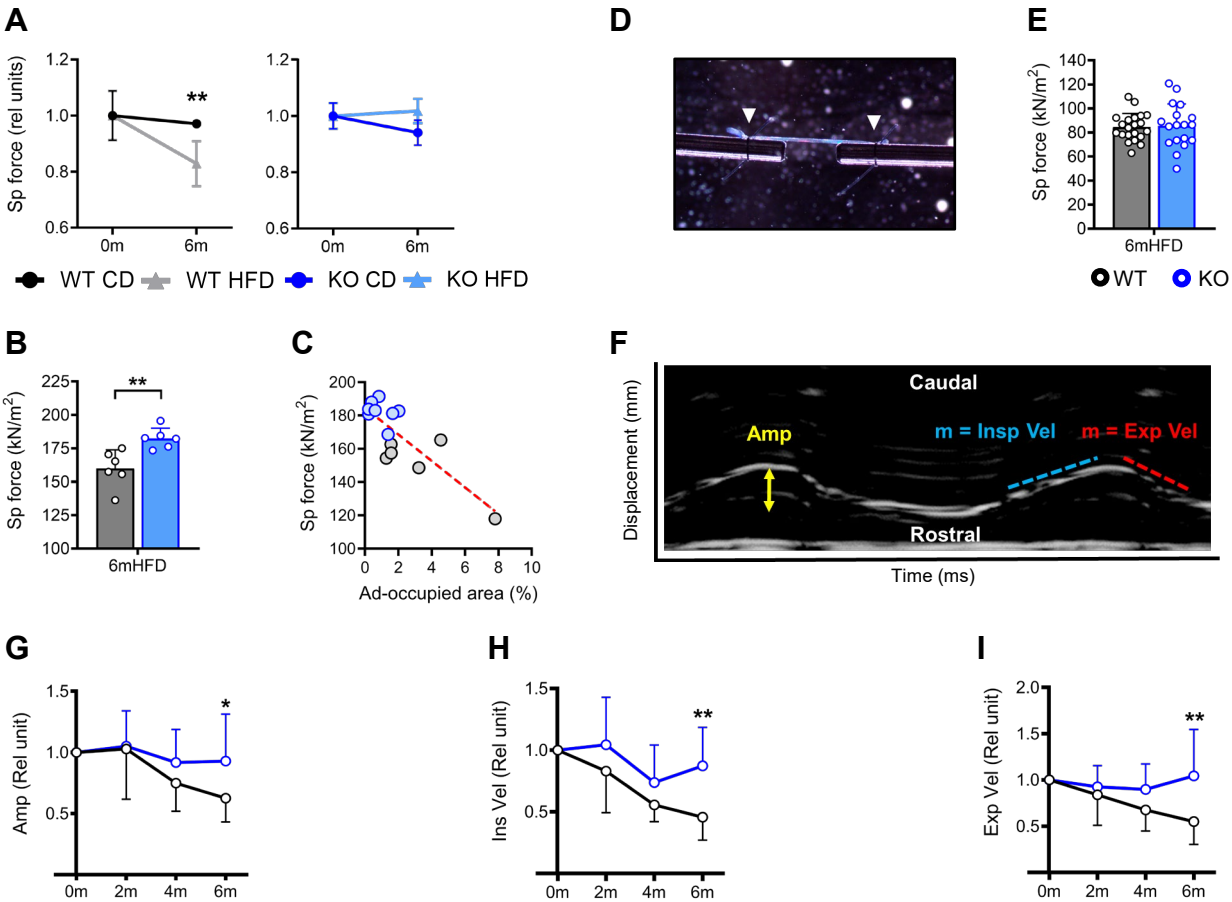


**Figure 6. DIO challenge compromises diaphragm force and motion in WT but not *Thbs1*$^{-/-}$ mice. (A)** Isometric specific force (Sp force) of wild-type (WT) and *Thbs1*$^{-/-}$ (KO) mice (normalized to baseline, relative units) at baseline (0m) and following 6-month (6m) control diet (CD) or high-fat diet (HFD) feeding. n= 4-6 animals per group; 1-2 diaphragm strips per animal averaged. **(B)** Isometric specific force (absolute value) of samples from 6m HFD WT and KO mice. n= 6 animals per group; 1-2 diaphragm strips per animal averaged. **(C)** Correlation plot demonstrating the relationship between isometric specific force and percent tissue cross-sectional area occupied by adipocytes in diaphragm strips subjected to isometric force testing. 6m HFD WT and KO mice, 8-9 individual muscle strips per group. **(D)** Image of single myofiber undergoing isometric force testing. White arrowheads indicate sutures affixing fiber to force transducer-servomotor apparatus. **(E)** Isometric specific force of single myofibers isolated from 6m HFD WT and KO mice (n= 4-5 animals per group; 4-5 fibers per animal). **(F)** Diaphragm ultrasound M-mode tracing with measured parameters labeled. x-axis represents time, y-axis represents displacement along the rostral-caudal axis. **(G-I)** Diaphragm motion parameters: amplitude (Amp), inspiratory velocity (Ins Vel), expiratory velocity (Exp Vel), normalized to baseline measured at 0m, 2m, 4m and 6m. n= 8-9 animals per group. Statistical analysis with t-test for individual comparisons and linear regression for correlational analysis. Error bars indicate SDM. *p<0.05, **p<0.01.